DOI: 10.1002/ ((please add manuscript number))
Article type: Full Paper

Elucidating the Sole Contribution from Electromagnetic Near-Fields in Plasmon-Enhanced Cu_2O Photocathodes

*Joseph S. DuChene, Benjamin P. Williams, Aaron C. Johnston-Peck, Jingjing Qiu, Mathieu Gomes, Maxime Amilhau, Donald Bejleri, Jiena Weng, Dong Su, Fengwei Huo, Eric A. Stach, and Wei David Wei**

J. S. DuChene, B. P. Williams, J. Qiu, M. Gomes, M. Amilhau, D. Bejleri, Prof. W. D. Wei
Department of Chemistry and Center for Nanostructured Electronic Materials, University of Florida, Gainesville, FL 32611, USA
E-mail: wei@chem.ufl.edu
Dr. A. C. Johnston-Peck, Dr. D. Su, Dr. E. A. Stach
Center for Functional Nanomaterials, Brookhaven National Laboratory, Upton, NY 11973, USA
Dr. J. Weng, Prof. F. Huo
Key Laboratory of Flexible Electronics and Institute of Advanced Materials, Jiangsu National Synergistic Innovation Center for Advanced Materials, Nanjing Tech University, Nanjing 211816, PR China

Keywords: cuprous oxide, photoelectrochemistry, solar energy conversion, surface plasmon resonance

Despite many promising reports of plasmon-enhanced photocatalysis, the inability to identify the individual contributions from multiple enhancement mechanisms has delayed the development of general design rules for engineering efficient plasmonic photocatalysts. Herein, we construct a plasmonic photocathode comprised of $Au@SiO_2$ (core@shell) nanoparticles embedded within a Cu_2O nanowire network to exclusively examine the contribution from one such mechanism: electromagnetic near-field enhancement. The influence of the local electromagnetic field intensity is correlated with the overall light-harvesting efficiency of the device through variation of the SiO_2 shell thickness (5—22 nm) to systematically tailor the distance between the plasmonic Au nanoparticles and the Cu_2O nanowires. A three-fold increase in device photocurrent is achieved upon integrating the $Au@SiO_2$ nanoparticles into the Cu_2O nanowire network, further enabling a ~40% reduction in semiconductor film thickness while maintaining photocathode performance. Photoelectrochemical results are further correlated with photoluminescence studies and optical simulations to confirm that the near-field enhancement is the sole mechanism responsible for increased light absorption in the plasmonic photocathode.

1. Introduction

Solar-driven water splitting via a photoelectrochemical cell represents a sustainable route to energy production by harvesting solar insolation and storing it in the form of chemical bonds (e.g. H_2).[1] Cuprous oxide (Cu_2O) is a promising p-type semiconductor for photoelectrochemical H_2 production as it consists of Earth-abundant elements, displays a direct optical band gap (E_g) suitable for solar energy conversion (E_g = 2.0 eV), and exhibits a so-called "built-in" overpotential for H_2 evolution.[2,3] Despite these auspicious properties, the performance of Cu_2O-based photocathodes is ultimately limited by the small optical cross section of this p-type oxide near the band edge.[2a–c] The abrupt decrease in Cu_2O absorption coefficient below 2.5 eV effectively narrows the spectral sensitivity of this ostensibly ~2.0 eV band gap semiconductor.[2a–c] Consequently, a significant portion of the solar spectrum (λ = 500—600 nm) theoretically available for driving H_2 evolution with a Cu_2O photocathode is often inefficiently harvested by the device.[2,3] Attempts to mitigate this constraint by fabricating thicker semiconductor films have met with limited success: such a strategy ultimately restricts device performance by adversely affecting charge carrier collection due to the incommensurate length scales between the optical penetration depth (α^{-1} = 1—3 μm) and the minority carrier diffusion length ($l_d \approx$ 50 nm).[2a,4] Innovative approaches to augment the optical cross section of the semiconductor without significantly altering the internal device architecture are therefore required to achieve viable solar-to-fuel conversion efficiencies.

Plasmonic-metal nanostructures (e.g. Au, Ag, Cu, Al, etc.) offer intriguing opportunities for solar photocatalysis due to their unique ability to confine freely propagating optical radiation into subwavelength volumes.[5,6] Optical excitation at their localized surface plasmon resonance (LSPR) frequency induces a local enhancement (~10^3) of electromagnetic (EM) fields near the nanoparticle (NP) surface that can markedly boost the absorption cross section of a nearby semiconductor photocatalyst.[5–7] Panchromatic light-harvesting devices are envisioned by tailoring the LSPR frequency to amplify the absorption profile of the semiconductor in regions of the solar spectrum that would otherwise be incompletely collected by the device.[8] While promising reports abound,[6,7] the pursuit of plasmonic photocatalysts is plagued by the daunting complexity of these systems.[5,6] Numerous plasmonic processes

may coexist spatiotemporally,[6,9] resigning most studies to invoke a multitude of mechanisms to explain the enhancements observed in the plasmonic composite. This inability to properly distinguish between different enhancement mechanisms has curtailed the development of a comprehensive set of plasmonic principles to guide the efficient augmentation of semiconductor-based devices with plasmonic-metal nanostructures.

Here, we construct a plasmon-enhanced photocathode composed of Au@SiO_2 (core@shell) NPs integrated within Cu_2O nanowire (NW) networks to exclusively evaluate the influence of plasmonic near-fields on the photoelectrochemical performance of a p-type semiconductor. To exclude resonant photon scattering, the plasmonic-metal core is comprised of a small Au NP possessing a negligible scattering cross section.[6,8a] Encapsulation within a dielectric silica (SiO_2) shell serves both to electrically isolate the metal NP from the Cu_2O NWs and to chemically isolate the Au NP surface from the surrounding electrolyte.[7a,8c] This core@shell motif therefore prevents direct charge transfer between the plasmonic-metal NPs and their surrounding environment while permitting the enhanced EM fields to permeate the dielectric shell and interact with the nearby semiconductor.[6] As the EM field intensity rapidly decays with increasing distance from the Au surface,[6] minor adjustments in SiO_2 shell thickness enable significant modulation of the local near-fields experienced by the Cu_2O NWs. Thus, our approach provides exquisite control over the physical proximity between material components at nanometer length scales to unambiguously elucidate the near-field contribution. This composite system (Cu_2O/Au@SiO_2) thereby constitutes an ideal test bed to systematically probe the sole influence of these plasmonic near-fields on a p-type semiconductor within a working photoelectrochemical cell. Our combined experimental and theoretical investigation demonstrates the merits of using plasmonic-metal nanostructures to boost the light-harvesting capability of a nearby semiconductor via the near-field mechanism. More importantly, the insights obtained from this systematic study aid in the eventual establishment of general plasmonic design rules for engineering efficient artificial photosynthetic constructs.

2. Results and Discussion

2.1. Cu_2O Nanowires.

The Cu_2O NWs were synthesized according to a hydrothermal method[10] that yields high aspect ratio NWs with diameters (d) of 80 ± 10 nm and typical lengths (l) of 10—25 μm (Figure S1, Supporting Information). Keeping the NW diameter (d = 80 nm) comparable to the minority carrier (e^-) diffusion length ($l_d \approx 50$ nm) is expected to facilitate diffusion to the semiconductor-liquid interface while maintaining an uninterrupted corridor for majority carrier (h^+) transport along the Cu_2O conduit.[4] Scanning electron microscopy (SEM) revealed that these NWs form large-scale interconnected networks on the fluorine-doped tin oxide (FTO) glass substrate, as shown in **Figure 1**a. The high internal surface area and large open channels of this interwoven structure are anticipated to facilitate electrolyte diffusion throughout the Cu_2O network during photoelectrochemical operation.[4] Further characterization of these materials with X-ray diffraction (Figure S2, Supporting Information) and Raman spectroscopy (Figure S3, Supporting Information) verified that these NWs were composed of the Cu_2O phase. The lattice planes of individual NWs were then indexed to those of Cu_2O by high-resolution transmission electron microscopy (HRTEM) and selected area electron diffraction (SAED) analysis (Figure S4, Supporting Information). Closer inspection of individual NWs by HRTEM revealed the presence of an amorphous layer ca. 1—2 nm thick adhered to the Cu_2O NW surface, as shown in Figure 1b,c. Subsequent investigation of the chemical composition of this amorphous layer by scanning transmission electron microscopy-electron energy loss spectroscopy (STEM-EELS) identified this substance to be highly enriched in carbon (C) and oxygen (O) relative to the Cu_2O NW core (Figure 1d—g and Figure S5, Supporting Information). We attribute the origin of this persistent carbon layer to the α-D-glucose used in the initial synthesis of the Cu_2O NWs.[10] It is noted that X-ray photoelectron spectroscopy (XPS) experiments also detected the presence of a carbon species on the Cu_2O NW surface (Figure S6, Supporting Information) consistent with glucose-derived carbon coatings.[9] This thin (~2 nm) carbon layer is anticipated to passivate the semiconductor surface during photoelectrochemical operation while permitting photogenerated charges to reach the solid-liquid junction and participate in chemical reactions.[3]

2.2. $Au@SiO_2$ (Core@Shell) Nanoparticles.

Small Au NPs (d = 10 ± 1 nm) served as the plasmonic-metal core for the subsequent deposition of conformal SiO_2 shells[11,12] of various thickness (5—25 nm) to yield Au@SiO_2 NPs (Figure S7, Supporting Information). Since it is expected that a near-field enhancement strategy will be most effective at wavelengths where the Cu_2O absorption coefficient is small (λ = 500—600 nm), spherical Au NPs exhibiting a maximum LSPR absorption (λ_{max}) at 521 nm were chosen to ensure sufficient spectral overlap with the optical response of the Cu_2O NWs (Figure S8, Supporting Information). As shown in **Figure 2**a, a slight red shift in λ_{max} was observed from 521 nm to 525 nm upon the deposition of a 5 ± 2 nm SiO_2 shell onto the Au NP core (inset of Figure 2a). This red shift is attributable to the increased refractive index of SiO_2 compared to H_2O.[12,13] After synthesis of the desired core@shell motif, these Au@SiO_2 NPs were intimately mixed with the Cu_2O NWs during device assembly to confer the maximum plasmonic enhancement to the Cu_2O/Au@SiO_2 photocathode.

2.3. Optical Properties.

The optical properties of these materials were characterized both in solution (solid lines) and in thin films (dashed lines), as shown in Figure 2b. The prominent extinction features present at ca. 463 nm and 480 nm are attributed to the interband transitions of the Cu_2O NWs (Figure 2b, solid red line). It is noted that the abrupt change in the optical cross-section of the Cu_2O NWs is evidenced by the steady decline in extinction towards longer wavelengths of the visible spectrum (λ = 500—600 nm). Although the optical extinction trails into the infrared (IR) regime, we attribute this feature to scattering rather than absorption, as no significant photoelectrochemical activity was observed for these Cu_2O photocathodes below λ_{inc} = 600 nm (*vide infra*). We therefore assign a band gap of ca. 2.0 eV to the Cu_2O NWs used in our study, in agreement with prior reports.[2,3] The near-IR scattering observed in solution was further exacerbated in the thin film samples due to the high optical density of the Cu_2O NW network on the FTO substrate (Figure 2b, dashed red line (i)).

The optical characteristics of the plasmonic composites (Cu_2O/Au@SiO_2) retain the peaks attributable to the interband transitions of the Cu_2O NWs, but exhibit an additional spectroscopic feature in the visible region centered at 525 nm due to the LSPR of the Au@SiO_2 NPs (Figure 2b, solid blue line).

Although the distinct optical properties from both components are easily discernable while mixed together in solution, these features were slightly obscured in the thin film samples (Figure 2b, dashed blue line). It is further noted that λ_{max} of the Au@SiO_2 NPs red-shifted to 534 nm in the composite device. Although the overall extinction throughout the entire visible spectrum was enhanced in the presence of the Au NPs, the most substantial improvements occurred in the spectral region commensurate with the LSPR of the Au NPs (λ = 500—600 nm), as shown by the difference spectrum in Figure 2b (black curve). This increased extinction at longer wavelengths imparts a more balanced absorption profile to the plasmonic system throughout the visible region than originally obtained with the Cu_2O-only device. These results suggest that the substantial optical cross section of the plasmonic NPs effectively augments the weak optical response of the Cu_2O NWs near the band edge (2.0—2.5 eV).

2.3. Photoelectrochemical Properties.

The photoelectrochemical properties of the photocathodes were then investigated via an electrochemical cell in a standard three-electrode configuration immersed in a supporting electrolyte composed of 0.10 M Na_2SO_4 (pH 6) (see Experimental section). The p-type Cu_2O photocathode served as the working electrode, with a Pt wire auxiliary electrode and a Ag/AgCl reference electrode. All electrode potentials (E) are reported relative to the Reversible Hydrogen Electrode (RHE). The photoelectrochemical stability of the Cu_2O NWs was first evaluated with the photocathodes potentiostatically poised at 0 V_{RHE} (V vs. RHE) while subjected to periodic (0.5 Hz) AM 1.5G irradiation at 3-sun intensity (I_0 = 300 ± 10 mW cm^{-2}) for 20 min. As shown in **Figure 3**a, the Cu_2O device displayed reproducible cathodic photocurrents (J_{ph} = −42 ± 2 μA cm^{-2}) over the course of the experiment, indicating superior photoelectrochemical stability relative to most Cu_2O-based photocathodes.[2] Although an initial decline in J_{ph} was observed at the onset (t = 0—60 s) of controlled potential electrolysis, this transient feature signifies the rapid depletion of protons near the electrode surface[4] rather than deterioration of the photocathode, as previous reports demonstrate that photocorrsion would manifest a continued decline in J_{ph} along the entire 20 min interval.[2,3] It was recently demonstrated that Cu_2O can be rendered electrochemically stable through passivation of the semiconductor surface with carbon-based coatings

derived from glucose precursors.[3] The considerable stability observed during controlled potential electrolysis over 20 min indicates that the α-D-glucose present during Cu_2O NW synthesis confers a similar carbon layer (Figure 1d—g) capable of stabilizing the semiconductor surface against photocorrosion. Inspection of the device after photoelectrochemical testing confirms the physicochemical stability of the Cu_2O-based photocathode employed herein (Figure S9, Supporting Information). These C-coated Cu_2O NWs thereby constitute the basis for a robust photoelectrochemical platform to study the EM near-field enhancement mechanism in p-type photocathodes.

A comparison of photoelectrochemical activity for the plasmonic device (Cu_2O/Au@SiO_2) and the control device (Cu_2O-only) is presented in Figure 3b—d. The Au@SiO_2 NPs with the thinnest SiO_2 shells of 5 ± 2 nm (Figure 2a, inset) were used for all plasmonic photocathodes unless otherwise specified (Figure S10, Supporting Information). The optimal Au@SiO_2 NP loading was empirically determined to be 0.5 ± 0.1 wt.% and was subsequently adopted for all photoelectrochemical experiments (Figure S11, Supporting Information). As shown in Figure 3b, the Cu_2O photocathodes were found to display a turn-on potential (E_{on}) of ca. 0.4 V_{RHE}, in agreement with previous reports.[2] The incorporation of the Au@SiO_2 NPs did not induce any change in E_{on} of the plasmonic device, but did impart a significant increase in J_{ph} along the potential sweep (Figure 3b). In particular, these voltammograms reveal a substantial J_{ph} enhancement at 0 V_{RHE} for the plasmonic device (J_{ph} = −29 ± 1 μA cm^{-2}) as compared to the control (J_{ph} = −9 ± 1 μA cm^{-2}). While both photocathodes displayed a linear J_{ph} dependence with respect to incident light intensity (I_0), it is noted that the plasmonic device delivered superior J_{ph} at any given power (~3 times more J_{ph}) relative to the Cu_2O-only photocathode (Figure S12, Supporting Information). Chronoamperometry experiments were then performed at an applied bias (E_{appl}) of 0 V_{RHE} to further demonstrate the reproducible 3-fold enhancement in J_{ph} for the plasmonic photocathode upon exposure to periodic (0.5 Hz) AM 1.5G irradiation at 1-sun intensity (Figure S13, Supporting Information). Controlled potential electrolysis experiments (E_{appl} = 0 V_{RHE}) conducted over a 20 min period confirm the

stability of these plasmonic photocathodes, indicating that no adverse effects arise from the incorporation of the Au@SiO_2 NPs within the Cu_2O NW network (Figure S14, Supporting Information).

Photocurrent action spectra [$J_{ph}(\lambda)$] were then acquired to correlate the photoelectrochemical response from the plasmonic and control photocathodes with their optical properties. A set of band pass filters (λ_{inc} = 400—700 nm, $\Delta\lambda$ = 20 nm ± 10 nm) were coupled with an AM 1.5G optical filter to assess the incident photon-to-current conversion efficiency (IPCE) of these photocathodes across the solar spectrum, as shown in Figure 3c. The IPCE of the control device qualitatively emulates the optical extinction of the Cu_2O NWs, although there was a significant decrease in IPCE for photon energies below 2.5 eV (Figure 3c, red points). We attribute this decline to the abrupt change in optical cross section for Cu_2O in this part of the visible spectrum (2.5—2.0 eV).[2] In contrast, the plasmonic device (Cu_2O/Au@SiO_2) displayed a more equitable absorption profile throughout the visible regime (Figure 3c, blue points). Notably, the largest improvements were engendered at wavelengths near the band edge of the Cu_2O NWs (λ = 500 to 600 nm), where the weak optical response of the semiconductor inhibits the efficient absorption of incident light. This enhancement in IPCE at wavelengths coincident with the LSPR of the Au NPs suggests a general strategy for incorporating plasmonic-metal nanostructures into light-harvesting devices to amplify the optical sensitivity of the semiconductor.

The incommensurate length scales required for simultaneously achieving sufficient light absorption (α^{-1} ~ μm) and efficient charge collection (l_d ~ nm) within a semiconductor film constitutes a significant challenge commonly encountered in photoelectrochemical cells.[1,4] Although increasing the Cu_2O NW loading increases the optical density of the semiconductor film (Figure S15, Supporting Information), it also extends the diffusion distance for excited-state charge carriers within the device.[4] Accordingly, a J_{ph} maximum was observed for a Cu_2O film thickness of ca. 3 μm in the control device (Figure 3d, red points). Assuming that the J_{ph} enhancement observed for the plasmonic photocathode occurs as a result of increased light absorption due to the Au@SiO_2 NPs, it is expected that the plasmonic device should require less Cu_2O material to achieve similar photoelectrochemical performance as the

control device. Indeed, the incorporation of Au@SiO_2 NPs into the Cu_2O NW network substantially shifted the J_{ph} maximum of the plasmonic device to lower Cu_2O loadings, obviating the need for ca. 40% of the photoactive material in the plasmonic device (Figure 3d, blue points). Such a significant reduction in material requirements demonstrates the possibility of supplementing semiconductor-based devices with plasmonic-metal nanostructures to boost the light harvesting capability of the photoactive layer while maintaining appropriate device dimensions to ensure efficient charge carrier collection (Figure S16, Supporting Information).

2.4. Photoluminescence Studies.

To confirm that the J_{ph} enhancements in the plasmonic device originate from increased light absorption due to the incorporation of the Au@SiO_2 NPs, the photoluminescence (PL) spectra of both control (Cu_2O-only) and plasmonic (Cu_2O/Au@SiO_2) devices were acquired and analyzed (see Experimental section). Assuming the PL emission originates solely from radiative recombination of photogenerated electron-hole (*e-h*) pairs within the semiconductor after optical excitation, examination of the PL spectrum provides a way to evaluate the light-harvesting efficiency of the device.[14] As the near-field EM mechanism is only operative at wavelengths where the optical absorption of the semiconductor and the LSPR of the plasmonic metal overlap,[6] a 532 nm laser (~2.3 eV) was used to ensure simultaneous excitation of both materials. A broad PL signal centered at ca. 2 eV was observed from the control device (Cu_2O-only) following irradiation with the 532 nm laser (Figure S17, Supporting Information), indicating that PL emission occurs primarily via free-carrier recombination near the band edge.[15] Significantly, the plasmonic device (Cu_2O/Au@SiO_2) displayed more than 3 times greater PL emission than the control device (Figure S17, Supporting Information). It must be emphasized that this PL enhancement shows close agreement to the J_{ph} enhancement (~3 times) observed via photoelectrochemical experiments (Figure 3b and Figure S13, Supporting Information). Such a direct correlation between the J_{ph} and PL enhancements strongly suggests that the improved photoelectrochemical performance observed in the plasmonic device is attributable to increased light-harvesting efficiency.

2.5. Mechanism Discussion.

The number of plasmonic enhancement mechanisms that must be considered depends upon the specific material properties of the individual building blocks comprising the plasmonic composite.[6] The four principle plasmonic enhancement mechanisms commonly invoked to explain the enhancements observed experimentally include: (1) resonant photon scattering, (2) hot electron transfer, (3) resonant energy transfer, and/or (4) local photothermal heating.[6] Mechanism (1) serves to increase the optical path length for resonant photons within the plasmonic-metal/semiconductor composite. This mechanism is only operative in systems containing large ($d \geq 50$ nm) plasmonic-metal nanostructures as the scattering cross section scales directly with the size of the metal NP.[6a,8a] Mechanism (2) harnesses the hot electron distribution generated on plasmonic-metal nanostructures during optical excitation to harvest visible light via a plasmonic photosensitization scheme analogous to that employed in dye-sensitized solar cells.[16] This approach requires intimate physical contact between the plasmonic metal and the semiconductor support in order to facilitate plasmon-mediated electron transfer (PMET) from the metal to the CB states of the adjacent semiconductor.[6] Mechanism (3) exploits the locally-enhanced EM fields near the surface of a plasmonic-metal nanostructure during excitation of its LSPR, since the optical transition rate of a semiconductor photocatalyst is proportional to the magnitude of these local EM fields ($|E|^2$).[6,7] This near-field mechanism requires that the LSPR frequency of the metal nanoparticle coincide with the threshold for bandgap excitation within the semiconductor to effectively couple incident light into these enhanced near-field modes.[6,7] Mechanism (4) occurs after the creation of hot *e-h* pairs via Landau damping.[9,17] This hot carrier distribution rapidly relaxes as it equilibrates with the metal lattice through electron-phonon coupling (t ~ps), thereby elevating the surface temperature of the metal nanoparticle relative to its environment.[9,17] This localized thermal energy is subsequently released to the nearby surroundings via heat transfer across the metal/solution interface (t ~ns).[9,17] It must be emphasized that these plasmonic processes may coexist in any given system,[6] requiring careful control over material components to conclusively elucidate the enhancement mechanism.

In the Cu_2O/Au@SiO_2 system employed here, the contribution from resonant photon scattering is negligible, since the small size of the Au NPs (d = 10 nm) substantially limits their scattering cross section.[6,8a] We also exclude increased photon scattering from the SiO_2 shell itself, as the integration of 12 nm SiO_2 NPs into the Cu_2O device (Cu_2O/SiO_2-only) had no significant effect on the J_{ph} of the photocathode (Figure S18a,b, Supporting Information). Additionally, the use of a dielectric SiO_2 shell to encapsulate the Au NP also precludes the possibility of PMET between the Au NPs and the Cu_2O NWs.[6] It is noted that the incorporation of 10 nm Au NPs without SiO_2 coating into the Cu_2O device (Cu_2O/Au-only) actually hindered the photoelectrochemical performance of the composite system (Figure S18c,d, Supporting Information). Subsequent PL measurements indicated that these metal NPs quench the excited-state of the Cu_2O NWs if not coated by a SiO_2 shell (Figure S19, Supporting Information). Local photothermal heating is also excluded due to the insulating SiO_2 shell that thermally isolates these metal nanostructures from their surroundings.[17] Therefore, the only likely plasmonic enhancement mechanism operative in the present system (Cu_2O/Au@SiO_2) must be associated with the presence of the enhanced near-fields generated by the Au NPs.

2.6. Elucidating the Enhancement Mechanism.

The signature of a near-field EM enhancement mechanism involves the rapid decay of device performance with increased separation distance between the plasmonic-metal nanostructure and the adjacent semiconductor.[6,18] To evaluate this proposed mechanism, the J_{ph} enhancements observed for the Au@SiO_2 NPs containing the thinnest SiO_2 shell (5 ± 2 nm) were compared to that of devices composed of Au@SiO_2 NPs with thicker SiO_2 shells of 9 ± 1 nm, 15 ± 1 nm, and 22 ± 2 nm (Figure S7 and Figure S20, Supporting Information). Indeed, **Figure 4** (red points) shows that the J_{ph} enhancement factor [J_{ph} EF = J_{ph}(plasmonic)/J_{ph}(control)] was increasingly attenuated as the silica shell thickness increased (where J_{ph} EF = 1 indicates no enhancement). Such a rapid decline in device performance indicates that the plasmonic enhancement is highly sensitive to the spatial separation between the Au NPs and the Cu_2O NWs.

The light absorption properties of these devices were then correlated with the J_{ph} enhancements by acquiring their PL spectra as a function of SiO_2 shell thickness (Figure S21, Supporting Information). As shown in Figure 4, a rapid decay in the PL EF was observed with increasing SiO_2 shell thickness (blue points) that was nearly identical to the trend observed for the J_{ph} EF obtained from photoelectrochemical measurements (red points). Such a striking similarity between the J_{ph} EF and the PL EF confirms that the improved photoelectrochemical performance of the plasmonic device is attributable to enhanced light absorption due to the incorporation of Au@SiO_2 NPs into the Cu_2O NW network. We also emphasize that the trends observed in both PL and J_{ph} enhancements are reminiscent of the well-known distance dependence of the EM field distribution around plasmonic-metal NPs under resonant optical excitation,[6] implicating the near-field EM mechanism.

Optical simulations were then performed within the context of the discrete dipole approximation (DDA)[19] to assess the influence of these near-fields on the adjacent Cu_2O NWs (see Supporting Information for computational details). The Au@SiO_2 NPs were modeled as concentric spheres immersed in a uniform dielectric medium (i.e. water) with physical dimensions congruent with those observed by HRTEM (Figure S7, Supporting Information). The spatial extent of the electric-field enhancement ($|E/E_0|^2$) around these Au@SiO_2 NPs under the incidence of visible light (λ = 525 nm) is shown in Figure S19, Supporting Information. As anticipated, the highest $|E/E_0|^2$ intensity was obtained for the Au@SiO_2 NPs with the thinnest SiO_2 shell of 5 nm (Figure S22, Supporting Information). The electric field enhancement at a fixed distance of 1 nm from the SiO_2 surface was then plotted as a function of SiO_2 shell thickness with the J_{ph} and PL enhancements to better correlate the theoretical trend with those of experiment (Figure 4, black points). There is a clear decrease in $|E/E_0|^2$ with increasing SiO_2 shell thickness, as the SiO_2 shell effectively modulates the distance between the enhanced EM fields from the Au NPs and their surrounding environment. Notably, the distance dependence of this field enhancement emulates the trends observed for both J_{ph} and PL EFs as a function of SiO_2 shell thickness, confirming that the photoelectrochemical performance is enhanced by this near-field mechanism. These spatially

inhomogeneous EM near-fields increase the optical transition rate within the adjacent semiconductor, thereby enhancing the photocatalytic reaction rate of the plasmonic composite.[5,6]

This systematic study establishes general plasmonic design rules for augmenting semiconductor-based devices with plasmonic-metal nanostructures. Our results show that a plasmonic enhancement strategy based upon the exploitation of these enhanced near-fields would be most successful at photon energies where the semiconductor exhibits a small optical cross section. It is noted that these plasmonic-metal nanostructures must be used sparingly, however, to minimize optical competition between material components for incident photons (Figure S11, Supporting Information). Therefore, it is important to consider the unique optical properties of different material building blocks in order to most effectively harvest incident light within a composite system. The ability to reduce the semiconductor film thickness by ca. 40% while maintaining device performance represents a significant step towards decoupling the light absorption efficiency from the charge carrier mobility of a semiconductor-based device. This near-field enhancement strategy is therefore expected to be particularly advantageous for materials plagued by poor minority carrier diffusion lengths since the photocatalytic reaction rate can be increased without adversely affecting the overall carrier collection efficiency of the device. The wide variety of anisotropic architectures accessible by wet-chemical synthesis suggests that such an approach could be employed within a multitude of light-harvesting systems to amplify the absorption profile in regions of the solar spectrum otherwise squandered by the device.[8] Taken together, these results demonstrate the potential opportunities provided by plasmonic-metal NPs for improving the light-harvesting efficiency of semiconductor-based devices for photoelectrochemical applications.

3. Conclusion

We have unambiguously isolated the EM near-field contribution from plasmonic-metal NPs on the light-harvesting efficiency of a p-type semiconductor via integration of $Au@SiO_2$ NPs into Cu_2O-based photocathodes. The plasmon-enhanced photocathodes ($Cu_2O/Au@SiO_2$) displayed increased IPCE at wavelengths commensurate with the LSPR of the Au NPs to yield a 3-fold increase in J_{ph} under simulated

sunlight as compared to the control photocathodes. These photoelectrochemical results were coupled with PL studies to verify that the improved device performance originated from increased light absorption within the Cu_2O NW network due to the introduction of the $Au@SiO_2$ NPs. Systematic attenuation of this device enhancement via manipulation of the SiO_2 shell thickness (5—22 nm) provided conclusive evidence that the increased light absorption was solely attributable to the locally enhanced EM fields generated by the Au NPs. Experimental results were further correlated with EM field simulations to confirm that the device enhancements occur via this near-field mechanism. Notably, we discovered that this approach enabled substantial improvements in light absorption within the photoactive layer while alleviating the requirement for thicker semiconductor films that often adversely affect charge carrier collection. We anticipate that these new insights will further the eventual establishment of a general set of design principles to guide the pursuit of plasmonic photocatalysts for efficient solar-to-fuel energy conversion.

4. Experimental Section

4.1. Materials.

Copper$^{(II)}$ sulfate ($CuSO_4$), trisodium citrate ($Na_3C_6H_5O_7$), and sodium hydroxide (NaOH) were purchased from Fisher Scientific (Hampton, NH). Sodium tartrate dibasic dihydrate ($Na_2C_4H_4O_6•2H_2O$), α-D-glucose ($C_6H_{12}O_6$), tetrachloroauric acid trihydrate ($HAuCl_4•3H_2O$), sodium borohydride ($NaBH_4$), L-ascorbic acid ($C_6H_8O_6$), hexadecyltrimethylammonium bromide (CTABr), tetraethoxysilane (TEOS), acetone (C_3H_6O), 2-propanol (C_3H_8O), and 12 nm SiO_2 NPs (No. 718483) were purchased from Sigma Aldrich (St. Louis, MO). The fluorine-doped tin oxide (FTO) glass substrates (TEC 15) were purchased from Hartford Glass Co. (Hartford City, IN). All materials were used as received without further purification. Nanopure© H_2O (Barnstead, 18.2 MΩ cm) was used for the preparation of all solutions. All glassware was cleaned with aqua regia solution and copious rinsing with Nanopure© H_2O prior to use. Caution! Aqua regia is highly corrosive and toxic: handle with care and use appropriate personal protection equipment.

4.2. Cu_2O Nanowire Synthesis.

The synthesis of Cu_2O nanowires (NWs) was conducted in accordance with a previous report.[10] Briefly, three aqueous solutions labeled Solution A, Solution B, and Solution C were freshly prepared in Nanopure© H_2O (18.2 MΩ cm). Solution A consists of a 2 mM $CuSO_4$ solution, Solution B is composed of 8 mM sodium tartrate in 14 mM NaOH (pH ~8) solution, and Solution C is a 0.1 mM α-D-glucose solution. The solutions were mixed together according to the volume ratio 1:1:2 (A:B:C) inside a 30 mL glass vial with a screw-on cap. The vials were sealed and placed in an oven and heated at 96° C for 75—90 min. After reaction, the solution was centrifuged three times at 10,000 RPM for 15 minutes and redispersed in Nanopure© H_2O for future use.

4.3. $Au@SiO_2$ Nanoparticle Synthesis.

The synthesis of Au nanoparticles (NPs) consisted of several steps and was based on two previous reports.[11,12] Initially, small Au NPs were created via the traditional $NaBH_4$ reduction of $HAuCl_4$ in the presence of sodium citrate to yield Au NP "seeds" with diameters of 3—5 nm. A subsequent seed-mediated growth step converted these small seeds into larger Au NPs via controlled secondary growth. A 9 mL growth solution composed of 10 mM CTABr and 0.25 mM $HAuCl_4$ was prepared, followed by the addition of 50 μL of freshly prepared 0.1 M ascorbic acid. After the growth solution turned colorless (~15 s) a 1 mL aliquot of the citrate-stabilized Au seeds was injected all at once under rapid magnetic stirring. This secondary growth step enlarges the Au NPs to 10 ± 1 nm in diameter, and they then serve as the substrate for the subsequent deposition of conformal silica (SiO_2) shells via our previously reported procedure.[12] Briefly, the 10 nm Au NPs were first centrifuged once for 15 min at 14,000 RPM and redispersed in Nanopure© H_2O. A 4 mL aliquot of these washed Au NPs was then added to a glass vial, followed by the addition of 100 μL of 1.0 M NaOH to raise the pH of the growth solution to pH ~10. The reaction was initiated by injecting 20 μL of tetraethoxysilane (TEOS) under rapid stirring. The addition of TEOS was repeated *x* times (where *x* = 1—8) in 60 min intervals to achieve a final SiO_2 shell thickness between 5—22 nm.

4.4. Photocathode Construction.

The p-type photocathodes were prepared by drop-casting the Cu_2O NW and $Au@SiO_2$ NP solutions onto clean FTO glass substrates. The FTO substrates were first cleaned via ultrasonication for 1 h in a solution of 1:1:1 (by volume) Nanopure© H_2O:2-propanol:acetone, then rinsed with Nanopure© H_2O, and finally dried with a stream of compressed air. All photoelectrochemical experiments were repeated in triplicate on three independently fabricated photocathodes. Device variability was minimized by using a single "master" solution of Cu_2O NWs at a fixed concentration for the preparation of all photocathodes. This approach enabled control over the Cu_2O film thickness (1—5 μm) by varying the total volume of solution that was drop-cast onto the substrate. Similarly, all plasmonic $Cu_2O/Au@SiO_2$ devices were prepared in triplicate from the same master Cu_2O NW solution used for control devices. The same methodology was applied for the plasmonic devices with a master $Au@SiO_2$ NP solution used for each different SiO_2 shell thickness investigated. This preparation method was adopted to minimize device variability (ca. 5%).

4.5. Materials Characterization.

Scanning electron microscopy (SEM) analysis of the Cu_2O NWs was conducted on an FEI Nova Nano 430 SEM operated at 15 kV and located at the Nanoscale Research Facility (NRF) at the University of Florida (UF). X-ray diffraction (XRD) patterns of the Cu_2O NWs on the FTO glass substrate were obtained using an X'Pert powder diffractometer (PANalytical Systems) with Cu Kα radiation (λ = 1.5406 Å) located at the Major Analytical Instrumentation Center (MAIC) at UF. Raman spectroscopy was performed using a Horiba Aramis Raman instrument using a 532 nm laser excitation wavelength located at NRF, UF. X-ray photoelectron spectroscopy (XPS) analysis of the Cu_2O NWs was conducted using a PHI 5000 *VersaProbe* II XPS instrument with a focused monochromatic Al Kα X-ray (1486.6 eV) source and a spherical section analyzer located at MAIC. A 50 W X-ray beam was focused to a 200 μm diameter spot size and incident normal to the sample with the photoelectron detector at 45° off-normal. Adventitious carbon (C) was used as a binding energy reference at 284.8 eV to correct for any specimen charging effect for all spectra. Structural analysis of the Cu_2O NWs was conducted by transmission electron microscopy (TEM) using a JEOL 200CX TEM and high-resolution transmission electron

microscopy (HRTEM) on a JEOL 2010F HRTEM (both instruments are located at MAIC). A 6 μL aliquot of Cu_2O NWs dispersed in Nanopure© H_2O was drop-cast onto a Holey Carbon 400 mesh Cu grid (Ted Pella, Inc.) and allowed to dry in ambient air prior to TEM or HRTEM analysis. Advanced materials characterization was carried out at the Center for Functional Nanomaterials at Brookhaven National Laboratory (BNL), Upton, NY. Additional HRTEM images of Cu_2O NWs were acquired using a JEOL 2100F HRTEM operated at 200 kV. Annular dark-field scanning transmission electron microscopy (ADF-STEM) imaging of Cu_2O NWs was conducted on a Cs-corrected Hitachi HD-2700C equipped with a Cold-FEG operated at 200 kV. Images were acquired using a probe convergence angle of 23 mrad and the inner collection angle of the ADF detector was 53 mrad. Electron Energy Loss Spectroscopy (EELS) mapping of the Cu_2O NWs was obtained using a Gatan Enfina spectrometer. The collection angle was set to 20 mrad with dispersions of 1.25 eV/ch or 0.3 eV/ch.

4.6. Photoelectrochemical Characterization.

The photoelectrochemical characteristics were investigated via the construction of a three-electrode electrochemical cell controlled by a potentiostat (EC Epsilon, Bioanalytical Systems, Inc.) with the Cu_2O NW photocathode serving as the working electrode (2 cm^2 area), a Ag/AgCl (saturated KCl) reference electrode, and a platinum (Pt) wire auxiliary electrode. All three electrodes were immersed in 0.10 M Na_2SO_4 (pH 6) as the supporting electrolyte. All potentials are reported relative to the Reversible Hydrogen Electrode (RHE), which represents the potential of the Standard Hydrogen Electrode (SHE) adjusted for the pH of the solution through the following equation:

$$E_{RHE} = E_{Ag/AgCl} + [0.059(pH)] + E^{\circ}_{Ag/AgCl}$$

where E_{RHE} is the converted potential vs. RHE, $E_{Ag/AgCl}$ is the experimental potential measured relative to the Ag/AgCl reference electrode, and $E^{\circ}_{Ag/AgCl}$ is the standard potential of the Ag/AgCl reference electrode relative to the RHE at 25 °C (0.1976 V_{RHE}). Photocathodes were illuminated through the FTO glass substrate with simulated sunlight using an ozone-free 300 W Xe lamp (Newport Corp.) equipped with an air mass (AM) 1.5G filter (Newport Corp.). It should be noted that all measurements were conducted at an incident power of $I_0 = 100 \pm 10$ mW cm^{-2} (1-sun intensity) unless otherwise indicated.

Prior to all photoelectrochemical experiments, the photocathodes were subjected to a mild heat treatment at 120 °C for 30 min to improve the adhesion between the NWs and the FTO glass substrate. The influence of applied bias on device photocurrent [$J_{ph}(E)$] was assessed under both steady-state light and dark conditions [$J_{ph}(E) = J_{light}(E) - J_{dark}(E)$] while a particular applied bias (E_{appl} = −0.50—1.4 V_{RHE}) was maintained by the potentiostat to exclude the influence of scan rate on device J_{ph}. Controlled potential electrolysis [$J_{ph}(t)$] and power-dependent photocurrent [$J_{ph}(I_0)$] experiments were conducted using the three-electrode configuration mentioned above while the photocathodes were poised at E_{appl} = 0 V_{RHE}. Incident photon-to-current conversion efficiency (IPCE) measurements were conducted using a set of band pass filters (λ = 400—700 nm) with a bandwidth of $\Delta\lambda$ = 20 nm ± 10 nm coupled to an AM 1.5G optical filter. The measured J_{ph} at each irradiation wavelength was then converted into an IPCE value according to the following equation:

$$\text{IPCE}\ (\%) = [(1240 \times J_{ph})/(I_0(\lambda) \times \lambda)] \times 100\%$$

where J_{ph} is the measured photocurrent density (in mA cm^{-2}), I_0 is the power density of the incident light (mW cm^{-2}) at a given wavelength, and λ is the wavelength of incident light (nm).

4.7. Photoluminescence Studies.

Photoluminescence (PL) spectra were collected on a Horiba Aramis Raman system using a 532 nm laser (grating of 1800 g mm^{-1}) to simultaneously excite the interband transitions within the Cu_2O NWs and the LSPR of the Au NPs. The samples were focused by a 100x objective lens. The laser spot size used for each measurement was ca. 5 μm in diameter with an incident power of 0.6 mW and an acquisition time of 5 s. PL spectra were acquired on pristine Cu_2O-only and Cu_2O/Au@SiO_2 devices prior to photoelectrochemical tests. All PL measurements were acquired from at least 9 randomly selected spots on each device and then averaged together to mitigate any sample heterogeneities caused by irregularities in film composition. Furthermore, each device condition was examined in duplicate to ensure accurate representation of the PL enhancement factor for the different SiO_2 shell thicknesses from 5 nm to 22 nm.

Supporting Information
Supporting Information is available from the Wiley Online Library or from the author.

Acknowledgements
The work is supported by the National Science Foundation (NSF) under grant DMR-1352328-CAREER, CHE-1308644, and the CCI Center for Nanostructured Electronic Materials (CHE-1038015). The XPS characterization was conducted using an instrument purchased with NSF grant MRI-DMR-1126115. M. G., M. A. and W. D. W. greatly appreciate the NSF-REU support from the iREU Site: The US/France REC Exchange Site in Chemistry (CHE-1156907). B. P. W. and D. B. acknowledge the generous support from Howard Hughes Medical Institute (HHMI) Intramural Award and the University Scholars Program at the University of Florida (UF). Materials characterization was primarily conducted at the Major Analytical Instrumentation Center and the Nanoscale Research Facility, College of Engineering Research Service Centers, UF. Electron microscopy work was carried out in part at the Center for Functional Nanomaterials at Brookhaven National Laboratory through User Proposals BNL-CFN-31913 and BNL-CFN-33789, supported by the U.S. Department of Energy, Office of Basic Energy Sciences, under Contract DE-SC0012704.

Received: ((will be filled in by the editorial staff))
Revised: ((will be filled in by the editorial staff))
Published online: ((will be filled in by the editorial staff))

[1] a) N. S. Lewis, D. G. Nocera, *Proc. Natl. Acad. Sci*. **2006**, *103*, 15729; b) M. G. Walter, E. L. Warren, J. R. McKone, S. W. Boettcher, Q. Mi, E. A. Santori, N. S. Lewis, *Chem. Rev.* **2010**, *110,* 6446; c) M. Grätzel, *Nature* **2001**, *414*, 338; d) Z. Peng, D. Jia, A. M. Al-Enizi, A. A. Elzatahry, G. Zheng, *Adv. Energy Mater.* **2015**, *5*, 1402031.

[2] a) A. Paracchino, J. C. Brauer, J.-E. Moser, E. Thimsen, M. Grätzel, *J. Phys. Chem. C* **2012**, *116*, 7341; b) P. E. de Jongh, D. Vanmaekelbergh, J. J. Kelly, *Chem. Commun.* **1999**, 1069; c) C. Xiang, G. M. Kimball, R. L. Grimm, B. S. Brunschwig, H. A. Atwater, N. S. Lewis, *Energy Environ. Sci.* **2011**, *4*, 1311; d) P. Bornoz, F. F. Abdi, S. D. Tilley, B. Dam, R. van de Krol, M. Grätzel, K. Sivula, *J. Phys. Chem. C* **2014**, *118,* 16959; e) A. Paracchino, V. Laporte, K. Sivula, M. Grätzel, E. Thimsen, *Nat. Mater.* **2011**, *10*, 456; f) A. Paracchino, N. Mathews, T. Hisatomi, M. Stefik, S. D. Tilley, M. Grätzel, *Energy Environ. Sci.* **2012**, *5*, 8673; g) S. D. Tilley, M. Schreier, J. Azevedo, M. Stefik, M. Grätzel, *Adv. Funct. Mater.* **2014**, *24*, 303; h) C. G. Morales-Guio, S. D. Tilley, H. Vrubel, M. Grätzel, X. Hu, *Nat. Commun.* **2014**, *5*, 3059; i) A. Azevedo, L. Steier, P. Dias, M. Stefik, C. T. Sousa, J. P. Araújo, A. Mendes, M. Grätzel, S. D. Tilley, *Energy Environ. Sci*. **2014**, *7*, 4044; j) C. Y. Lin, Y. H. Lai, D. Mersch, E. Reisner,

Chem. Sci. **2012**, *3*, 3482; k) J. Han, X. Zong, X. Zhou, C. Li, *RSC Adv.* **2015**, *5*, 10790; l) P. Dai, W. Li, J. Xie, Y. He, J. Thorne, G. McMahon, J. Zhan, D. Wang, *Angew. Chem. Int. Ed.* **2014**, *53*, 13493; *Angew. Chem.* **2014**, *126*, 13711.

[3] a) Z. Zhang, R. Dua, L. Zhang, H. Zhu, H. Zhang, P. Wang, *ACS Nano,* **2013**, *7*, 1709; b) J. Hou, C. Yang, H. Cheng, S. Jiao, O. Takeda, H. Zhu, *Energy Environ. Sci.* **2014**, *7*, 3758.

[4] a) M. Liu, N. de Leon Snapp, H. Park, *Chem. Sci.* **2011**, *2*, 80; b) L. Li, Y. Yu, F. Meng, Y. Tan, R. J. Hamers, S. Jin, *Nano Lett*. **2012**, *12*, 724; c) D. Bae, T. Pedersen, B. Seger, M. Malizia, A. Kuznetsov, O. Hansen, I. Chorkendorff, P. C. K. Vesborg, *Energy Environ. Sci.* **2015**, *8*, 650.

[5] a) J. A. Schuller, E. S. Barnard, W. Cai, Y. C. Jun, J. S. White, M. L. Brongersma, *Nat. Mater.* **2010**, *9*, 193; b) L. Novotny, N. van Hulst, *Nat. Photon.* **2011**, *5*, 83; c) W. L. Barnes, A. Dereux, T. W. Ebbesen, *Nature* **2003**, *424*, 824.

[6] a) S. Linic, P. Christopher, D. B. Ingram, *Nat. Mater.* **2011**, *10*, 911; b) S. C. Warren, E. Thimsen, *Energy Environ. Sci*. **2012**, *5*, 5133; c) W. Hou, S. B. Cronin, *Adv. Funct. Mater.* **2013**, *23*, 1612; d) D. B. Ingram, P. Christopher, J. L. Bauer, S. Linic, *ACS Catal*. **2011**, *1*, 1441; e) B. Jiang, B. Li, C. Fang, J. Wang, *Adv. Mater.* **2014**, *26*, 5274.

[7] a) S. K. Cushing, J. Li, F. Meng, T. R. Senty, S. Suri, M. Zhi, M. Li, A. D. Bristow, N. Wu, *J. Am. Chem. Soc.* **2012**, *134*, 15033; b) Z. Liu, W. Hou, P. Pavaskar, M. Aykol, S. B. Cronin, *Nano Lett.* **2011**, *11*, 1111; c) I. Thomann, B. A. Pinaud, Z. Chen, B. M. Clemens, T. F. Jaramillo, M. L. Brongersma, *Nano Lett.* **2011**, *11,* 3440; d) D. B. Ingram, S. Linic, *J. Am. Chem. Soc.* **2011**, *133*, 5202; e) H. Gao, C. Liu, H. E. Jeong, P. Yang, *ACS Nano* **2012**, *6*, 234; f) E. Thimsen, F. Le Formal, M. Grätzel, S. C. Warren, *Nano Lett.* **2011**, *11*, 35; g) L. Wang, J. Ge, A. Wang, M. Deng, X. Wang, S. Bai, R. Li, J. Jiang, Q. Zhang, Y. Luo, Y. Xiong, *Angew. Chem. Int. Ed.* **2014**, *53*, 5107; *Angew. Chem.* **2014**, *126*, 5207; h) D. O. Sigle, L. Zhang, S. Ithurria, B. Dubertret, J. J. Baumberg, *J. Phys. Chem. Lett.* **2015**, *6*, 1099; i) L. Zhang, C.-Y. Lin, V. K. Valev, E. Reisner, U. Steiner, J. J. Baumberg, *Small*, **2014**, *10*, 3970; j) F. F. Abdi, A. Dabirian, B. Dam, R. van de Kroel, *Phys. Chem. Chem. Phys.* **2014**, *16*, 15272; k) J. Qiu, G.

Zeng, P. Pavaskar, Z. Li, S. B. Cronin, *Phys. Chem. Chem. Phys.* **2014**, *16*, 3115; l) H. J. Kim, S. H. Lee, A. A. Upadhye, I. Roo, M. I. Tejedor-Tejedor, M. A. Anderson, W. B. Kim, G. W. Huber, *ACS Nano* **2014**, *8*, 10756; m) H. M. Chen, C. K. Chen, C.-J. Chen, L.-C. Cheng, P. C. Wu, B. H. Cheng, Y. Z. Ho, M. L. Tseng, Y.-Y. Hsu, T.-S. Chan, J.-F. Lee, R.-S. Liu, D. P. Tsai, *ACS Nano* **2012**, *6*, 7362; n) J. Li, S. K. Cushing, P. Zheng, F. Meng, D. Chu, N. Wu, *Nat. Commun.* **2013***, 4*, 2651; o) J. Wang, S. Pan, M. Chen, D. A. Dixon, *J. Phys. Chem. C* **2013**, *117*, 22060; p) Y. Tang, Z. Jiang, G. Xing, A. Li, P. D. Kanhere, Y. Zhang, T. C. Sum, S. Li, X. Chen, Z. Dong, Z. Chen, *Adv. Funct. Mater.* **2013**, *23*, 2932; q) S. Ramadurgam, T.-G. Lin, C. Yang, *Nano Lett.* **2014**, *14*, 4517; r) T. Tachikawa, T. Yonezawa, T. Majima, *ACS Nano* **2013**, *7*, 263; s) P. Da, W. Li, X. Lin, Y. Wang, J. Tang, G. Zheng, *Anal. Chem.* **2014**, *86*, 6633.

[8] a) H. A. Atwater, A. Polman, *Nat. Mater.* **2010**, *9,* 205; b) M. D. Brown, T. Suteewong, R. S. S. Kumar, V. D'Innocenzo, A. Petrozza, M. Lee, U. Wiesner, H. J. Snaith, *Nano Lett*. **2011**, *11*, 438; c) J. Qi, X. Dang, P. T. Hammond, A. M. Belcher, *ACS Nano* **2011**, *5*, 7108; d) X. Dang, J. Qi, M. T. Klug, P. Y. Chen, D. S. Yun, N. X. Fang, P. T. Hammond, A. M. Belcher, *Nano Lett.* **2013**, *13*, 637; e) D. H. Lee, J. Y. Kwon, S. Maldonado, A. Tuteja, A. Boukai, *Nano Lett.* **2014**, *14*, 1961; f) M. Chen, L. Shao, S. V. Kershaw, H. Yu, J. Wang, A. L. Rogach, N. Zhao, *ACS Nano* **2014**, *8*, 8208.

[9] a) G. V. Hartland, *Chem. Rev.* **2011**, *111*, 3858; b) K. Watanabe, D. Menzel, N. Nilius, H.-J. Freund, *Chem. Rev.* **2006**, *106*, 4301; c) S. Link, M. A. El-Sayed, *J. Phys. Chem. B* **1999**, *103*, 8410.

[10] S. Hacialioglu, F. Meng, S. Jin, *Chem. Commun.* **2012**, *48*, 1174.

[11] N. R. Jana, L. Gearheart, C. J. Murphy, *Langmuir* **2001**, *17*, 6782.

[12] J. S. DuChene, R. P. Almeida, W. D. Wei, *Dalton Trans*. **2012**, *41*, 7879.

[13] J. Rodríguez-Fernández, I. Pastoriza-Santos, J. Pérez-Juste, F. J. García de Abajo, L. M. Liz-Marzán, *J. Phys. Chem. C* **2007**, *111*, 13361.

[14] a) J. L. Wu, F. C. Chen, Y. S. Hsiao, F. C. Chien, P. Chen, C. H. Kuo, M. H. Huang, C. S. Hsu, *ACS Nano* **2011**, *5*, 959; b) W. Zhang, M. Saliba, S. D. Stranks, Y. Sun, X. Shi, U. Wiesner, H. J. Snaith,

Nano Lett. **2013**, *13*, 4505; c) T. Takahashi, A. Kudo, S. Kuwabata, A. Ishikawa, H. Ishihara, Y. Tsuboi, Y. Torimoto, *J. Phys. Chem. C* **2013**, *117*, 2511.

[15] a) L. S. Shinde, K. K. Nanda, *RSC Adv.* **2012**, *2*, 3647; b) H. Shi, K. Yu, F. Sun, Z. Zhu, *CrystEngComm* **2012**, *14*, 278.

[16] a) C. G. Silva, R. Juárez, T. Marino, R. Molinari, H. García, *J. Am. Chem. Soc*. **2011**, *133*, 595; b) J. Lee, S. Mubeen, X. Ji, G. D. Stucky, M. Moskovits, *Nano Lett.* **2012**, *12*, 5014; c) S. Mubeen, J. Lee, N. Singh, S. Kramer, G. D. Stucky, M. Moskovits, *Nat. Nanotechnol.* **2013**, *8*, 247; d) X. Wang, C. Liow, A. Bisht, X. Liu, T. C. Sum, X. Chen, S. Li, *Adv. Mater.* **2015**, *27*, 2207; e) J. S. DuChene, B. C. Sweeny, A. C. Johnston-Peck, D. Su, E. A. Stach, W. D. Wei, *Angew. Chem. Int. Ed.* **2014**, *53*, 7887; *Angew. Chem.* **2014**, *126*, 8021; f) Y. C. Pu, G. Wang, K. D. Chang, Y. Ling, Y. K. Lin, B. C. Fitzmorris, C. M. Liu, X. Lu, Y. Tong, J. Z. Zhang, Y. J. Hsu, Y. Li, *Nano Lett*. **2013**, *13*, 3817; g) K. Qian, B. C. Sweeny, A. C. Johnston-Peck, W. Niu, J. O. Graham, J. S. DuChene, J. Qiu, Y. C. Wang, M. H. Engelhard, D. Su, E. A. Stach, W. D. Wei, *J. Am. Chem. Soc.* **2014**, *136*, 9842; h) Y. Zhong, K. Ueno, Y. Mori, X. Shi, T. Oshikiri, K. Murakoshi, H. Inoue, H. Misawa, *Angew. Chem. Int. Ed.* **2014**, *53*, 10350; *Angew. Chem.* **2014**, *126*, 10518; i) M. L. Brongersma, N. J. Halas, P. Nordlander, *Nat. Nanotechnol.* **2015**, *10*, 25; j) A. Manjavacas, J. G. Liu, V. Kulkarni, P. Nordlander, *ACS Nano* **2014**, *8*, 7630; k) R. Sundararaman, P. Narang, A. S. Jermyn, W. A. Goddard III, H. A. Atwater, *Nat. Commun.* **2015**, *5*, 5788; l) Y. Nishijima, K. Ueno, Y. Kotake, K. Murakoshi, H. Inoue, H. Misawa, *J. Phys. Chem. Lett.* **2012**, *3*, 1248; m) Y. Kang, S. Najmei, Z. Liu, Y. Bao, Y. Wang, X. Zhu, N. J. Halas, P. Nordlander, P. M. Ajayan, J. Lou, Z. Fang, *Adv. Mater.* **2014**, *26*, 6467; n) B. Li, T. Gu, T. Ming, J. Wang, P. Wang, J. Wang, J. C. Yu, *ACS Nano* **2014**, *8*, 8152; o) C. Clavero, *Nat. Photon.* **2014**, *8*, 95; p) S. Bai, X. Li, Q. Kong, R. Long, C. Wang, J. Jiang, Y. Xiong, *Adv. Mater.* **2015**, *27*, 3444; q) R. Long, K. Mao, M. Gong, S. Zhou, J. Hu, M. Zhi, Y. You, S. Bai, J. Jiang, Q. Zhang, X. Wu, Y. Xiong, *Angew. Chem. Int. Ed.* **2014**, *53*, 3205; *Angew. Chem.* **2014**, *126*, 3269; r) Z. Bian, T. Tachikawa, P. Zhang, M. Fujitsuka, T. Majima, *J. Am. Chem. Soc.* **2014**, *136*, 458; s) S. Bai, J. Jiang, Q. Zhang, Y. Xiong, *Chem. Soc. Rev.* **2015**, *44*, 2893.

[17] a) J. Qiu, W. D. Wei, *J. Phys. Chem. C* **2014**, *118*, 20735; b) H. Chen, L. Shao, T. Ming, Z. Sun, C. Zhao, B. Yang, J. Wang, *Small* **2010**, *6*, 2272; c) F. Wang, C. Li, H. Chen, R. Jiang, L.-D. Sun, Q. Li, J. Wang, J. C. Yu, C.-H. Yan, *J. Am. Chem. Soc.* **2013**, *135*, 5588.

[18] a) S. D. Standridge, G. C. Schatz, J. T. Hupp, *J. Am. Chem. Soc.* **2009**, *131*, 8407; b) M. K. Kumar, S. Krishnamoorthy, L. K. Tan, S. Y. Chiam, S. Tripathy, H. Gao, *ACS Catal.* **2011**, *1*, 300; c) P. Reineck, D. Gomez, S. H. Ng, M. Karg, T. Bell, P. Mulvaney, U. Bach, *ACS Nano* **2013**, *7*, 6636; d) N. S. Abadeer, M. R. Brennan, W. L. Wilson, C. J. Murphy, *ACS Nano* **2014**, *8*, 8392; e) S. Jin, E. DeMarco, M. J. Pellin, O. K. Farha, G. P. Wiederrecht, J. T. Hupp, *J. Phys. Chem. Lett.* **2013**, *4*, 3527.

[19] a) E. M. Purcell, C. R. Pennypacker, *Astrophys. J.* **1973**, *186*, 705; b) B. T. Draine, *Astrophys. J.* **1988**, *333*, 848.

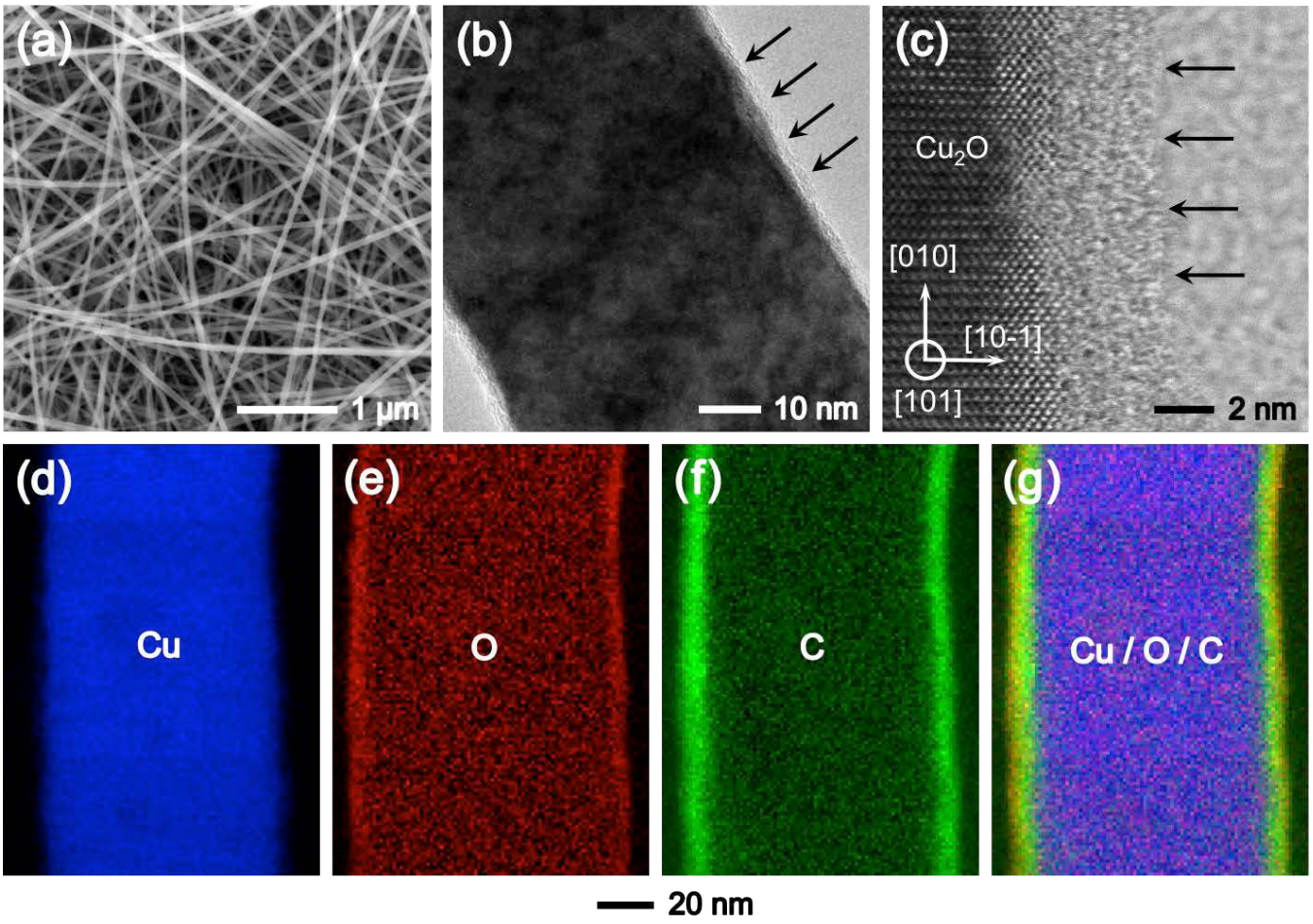

Figure 1. Materials characterization of Cu_2O nanowires used for the fabrication of p-type photocathodes. a) SEM image of a p-type photocathode comprised of Cu_2O nanowires deposited on a fluorine-doped tin oxide (FTO) glass substrate. b,c) HRTEM images of a single nanowire with crystal planes indexed to the Cu_2O phase. Arrows highlight the amorphous carbon layer observed on the surface of these nanowires. d—g) STEM-EELS elemental mapping of a single Cu_2O nanowire showing EELS signals from d) copper (Cu - blue), e) oxygen (O - red), f) carbon (C - green), and g) overlay of all three signals (Cu/O/C); the 20 nm scale bar applies to all EELS maps (d—g).

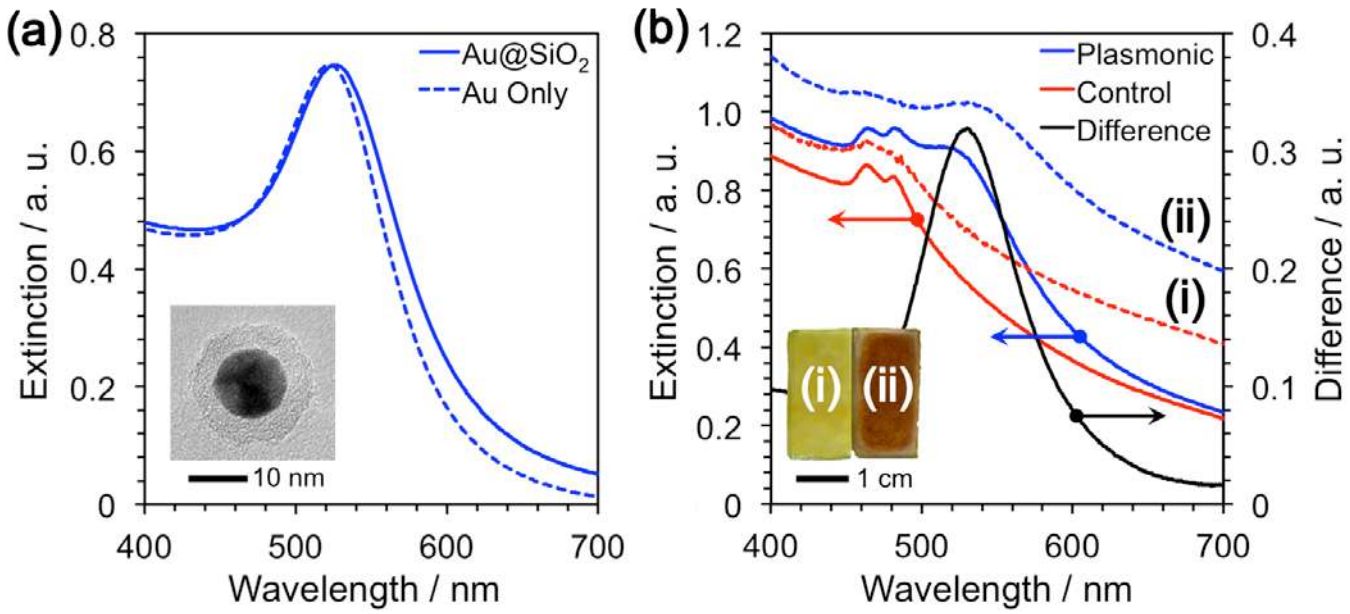

Figure 2. Optical properties of materials used for the fabrication of control Cu_2O-only (red) and plasmonic $Cu_2O/Au@SiO_2$ (blue) photocathodes. a) Extinction spectra of Au nanoparticles (dashed blue curve) and $Au@SiO_2$ nanoparticles (solid blue curve) in aqueous solution. Inset shows a TEM image of a typical $Au@SiO_2$ nanoparticle. b) Extinction spectra of Cu_2O nanowires in solution (solid red line) and a mixture of Cu_2O nanowires with $Au@SiO_2$ nanoparticles dispersed in solution (solid blue line). A difference spectrum (solid black line) shows the increased extinction in the visible spectrum (500-600 nm) due to the $Au@SiO_2$ nanoparticles. The extinction spectra of the Cu_2O-only film (dashed red line) and the $Cu_2O/Au@SiO_2$ composite film (dashed blue line) are also shown for comparison. Inset shows a digital image of the (i) Cu_2O-only and (ii) $Cu_2O/Au@SiO_2$ films on the FTO glass substrate.

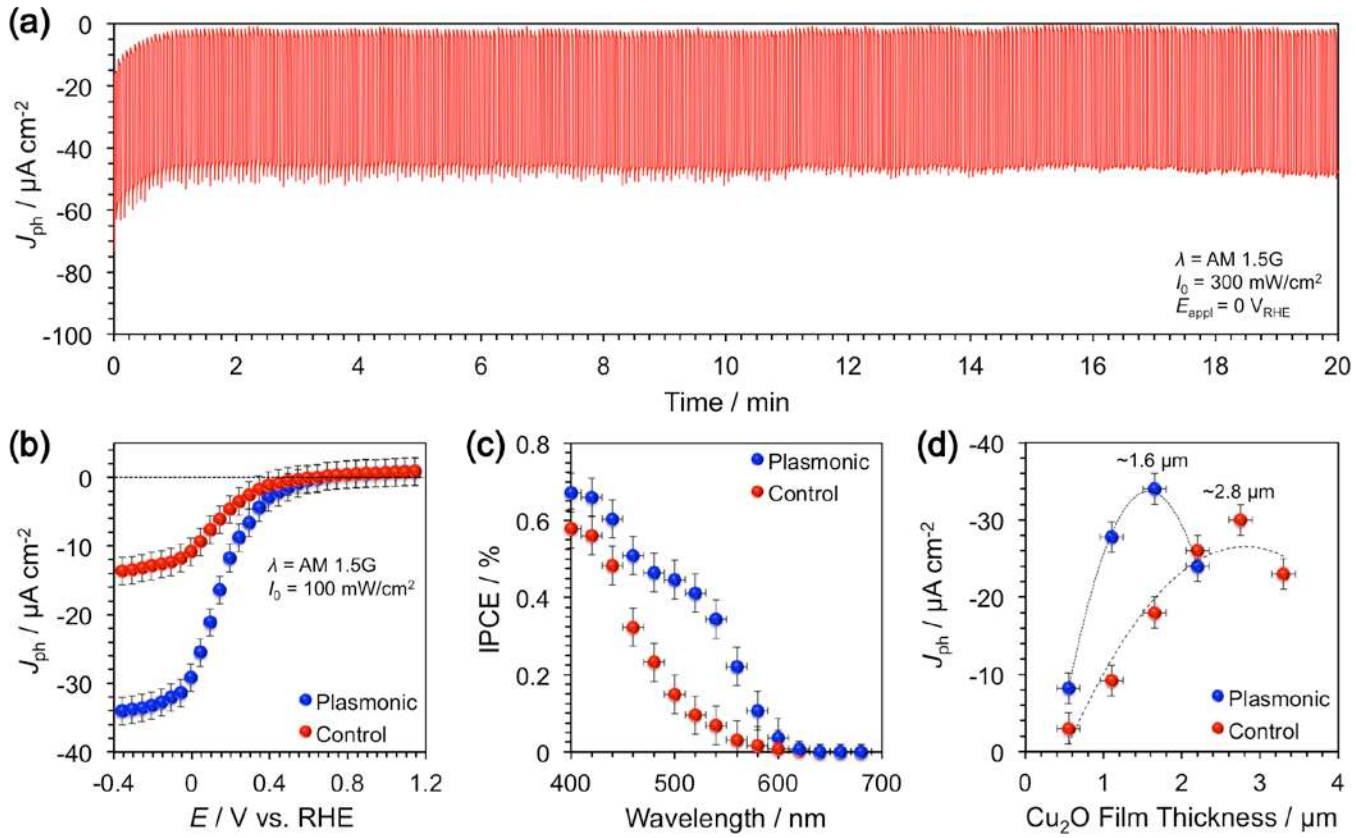

Figure 3. Photoelectrochemical properties of control Cu_2O-only (red) and plasmonic Cu_2O/Au@SiO_2 (blue) photocathodes. a) Controlled potential electrolysis of Cu_2O-only photocathodes poised at an applied bias (E_{appl}) of 0 V_{RHE} while exposed to periodic (2 s on/off) AM 1.5G illumination over a 20 min period. b) Influence of electrode potential (E) on device photocurrent (J_{ph}). c) Incident photon-to-charge conversion efficiency (IPCE) action spectra of photocathodes (E_{appl} = 0 V_{RHE}). d) Influence of Cu_2O film thickness on device J_{ph} under 1-sun AM 1.5G irradiation (E_{appl} = 0 V_{RHE}).

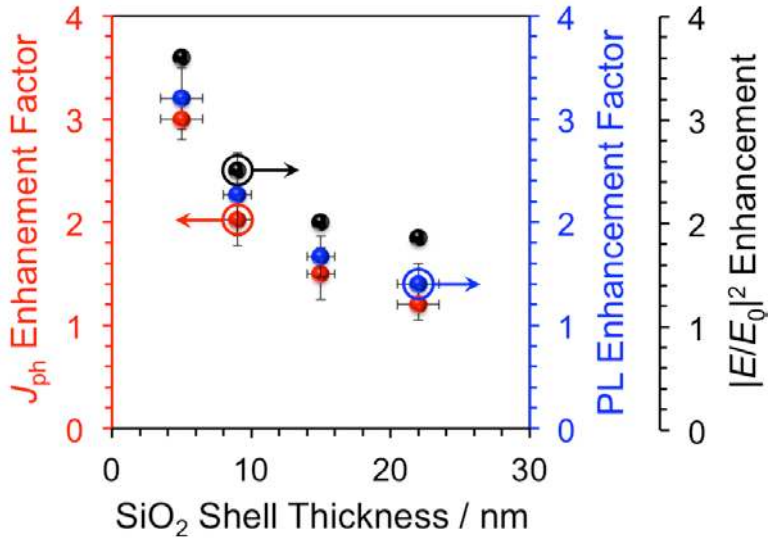

Figure 4. Correlating the experimental results with the plasmonic near-fields. Influence of Au-Cu_2O separation distance (modulated by SiO_2 shell thickness) on the photocurrent (J_{ph}, red), photoluminescence (PL, blue), and electromagnetic field ($|E/E_0|^2$, black) enhancement factors (EFs) for the plasmonic (Cu_2O/Au@SiO_2) photocathodes containing Au@SiO_2 nanoparticles of different SiO_2 shell thicknesses (5—22 nm).

Cu_2O photocathodes are augmented with Au@SiO_2 core-shell nanoparticles to exclusively evaluate the electromagnetic near-field enhancement mechanism in a p-type photocathode. Direct correlation between theory and experiment unambiguously demonstrates the sole influence of plasmonic near-fields on the light-harvesting efficiency of a semiconductor photoelectrode and elucidates general design rules for the rational construction of plasmonic photocatalysts.

Plasmon-enhanced Photoelectrochemistry

J. S. DuChene, B. P. Williams, A. C. Johnston-Peck, J. Qiu, M. Gomes, M. Amilhau, D. Bejleri, J. Weng, D. Su, F. Huo, E. A. Stach, and W. D. Wei*

Elucidating the Sole Contribution from Electromagnetic Near-Fields in Plasmon-Enhanced Cu_2O Photocathodes

ToC figure

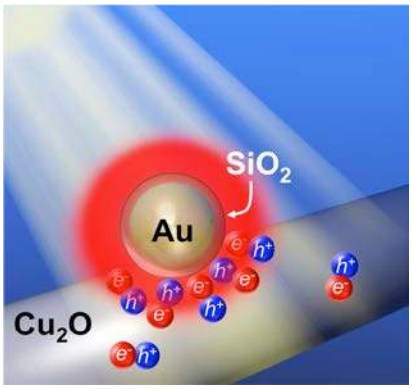

Supporting Information

Elucidating the Sole Contribution from Electromagnetic Near-Fields in Plasmon-Enhanced Cu_2O Photocathodes

*Joseph S. DuChene, Benjamin P. Williams, Aaron C. Johnston-Peck, Jingjing Qiu, Mathieu Gomes, Maxime Amilhau, Donald Bejleri, Jiena Weng, Dong Su, Fengwei Huo, Eric A. Stach, and Wei David Wei**

Experimental Procedures

Materials

Copper$^{(II)}$ sulfate ($CuSO_4$), trisodium citrate ($Na_3C_6H_5O_7$), and sodium hydroxide (NaOH) were purchased from Fisher Scientific (Hampton, NH). Sodium tartrate dibasic dihydrate ($Na_2C_4H_4O_6 \bullet 2H_2O$), α-D-glucose ($C_6H_{12}O_6$), tetrachloroauric acid trihydrate ($HAuCl_4 \bullet 3H_2O$), sodium borohydride ($NaBH_4$), L-ascorbic acid ($C_6H_8O_6$), hexadecyltrimethylammonium bromide (CTABr), tetraethoxysilane (TEOS), acetone (C_3H_6O), 2-propanol (C_3H_8O), and 12 nm SiO_2 NPs (No. 718483) were purchased from Sigma Aldrich (St. Louis, MO). The fluorine-doped tin oxide (FTO) glass substrates (TEC 15) were purchased from Hartford Glass Co. (Hartford City, IN). All materials were used as received without further purification. Nanopure© H_2O (Barnstead, 18.2 MΩ cm) was used for the preparation of all solutions. All glassware was cleaned with aqua regia solution and copious rinsing with Nanopure© H_2O prior to use. Caution! Aqua regia is highly corrosive and toxic: handle with care and use appropriate personal protection equipment.

Synthesis of Cu_2O Nanowires

The synthesis of Cu_2O nanowires (NWs) was conducted in accordance with a previous report.[1] Three aqueous solutions labeled Solution A, Solution B, and Solution C were freshly prepared in Nanopure© H_2O (18.2 MΩ cm) each day the synthesis was conducted. Solution A

was a 2 mM $Cu^{(II)}SO_4$ solution, Solution B was composed of 8 mM sodium tartrate in 14 mM NaOH (pH ~8) solution, and Solution C was a 0.1 mM α-D-glucose solution. The solutions were mixed together according to the volume ratio 1:1:2 (A:B:C) in 5:5:10 mL volumes inside a 30 mL glass vial with a screw-on cap. The vials were sealed and placed in an oven and heated at 96° C for 75—90 min. After this time, the solution changed color from a pale blue solution to a vibrant yellow color, signifying the reduction of $Cu^{(II)}$ to $Cu^{(I)}$ and the growth of Cu_2O NWs. The vials were removed from the oven, allowed to cool naturally to room temperature (~1 h), centrifuged three times at 10,000 RPM for 15 minutes to clean Cu_2O NWs, and finally redispersed in Nanopure© H_2O for future use. This procedure was repeated many times to compile enough NWs for the eventual fabrication of Cu_2O NW-based photocathodes.

Synthesis of Au@SiO_2 (Core@Shell) Nanoparticles

The synthesis of Au nanoparticles (NPs) consisted of several steps, and was based on two previous reports.[2,3] Initially, small Au NPs were created via the traditional $NaBH_4$ reduction of $HAuCl_4$ in the presence of sodium citrate to yield small Au NP "seeds" with diameters of 3-5 nm.[2] The Au seed solution was prepared by adding 1 mL of 10 mM $HAuCl_4$ and 1 mL of 10 mM sodium citrate to 37 mL of Nanopure© H_2O in a glass beaker. A 1 mL aliquot of an ice-cold 100 mM $NaBH_4$ solution was then added all at once to this solution under vigorous stirring and allowed to react for 2—3 h prior to use. A subsequent seed-mediated growth step converted these small seeds into larger Au NPs via controlled secondary growth according to a previous literature report,[2] but with slight modification. A 9 mL growth solution composed of 10 mM CTABr and 0.25 mM $HAuCl_4$ was then prepared in a 16 mL glass vial, followed by the addition of 50 μL of 0.1 M ascorbic acid (freshly prepared) under rapid magnetic stirring. After the solution turned colorless, signifying the reduction of $Au^{(III)}$ to $Au^{(I)}$, a 1 mL aliquot of the citrate-stabilized Au seeds was injected all at once under rapid magnetic stirring. The reaction was allowed to proceed for 10—20 min until a vibrant

purple color is achieved, at which point the stir bar was removed and the solution was stored for further use. This secondary growth step enlarges the Au NPs to 10 ± 1 nm in diameter, and these NPs then serve as the substrate for the subsequent deposition of silica (SiO_2) shells. We note that our procedure uses a 10 mM CTABr growth solution instead of the 100 mM CTABr solution initially reported[2] because we found that this lower concentration allows for controlled enlargement of the Au NPs without the concomitant production of unwanted Au nanorods.[3] Conformal SiO_2 shells were then deposited onto the Au NP surface via our previously reported procedure.[3] Briefly, the 10 nm Au NPs were first centrifuged once for 15 min at 14,000 RPM and redispersed in Nanopure© H_2O to remove excess CTABr from the solution (a critical step for achieving conformal SiO_2 shells).[3] A 4 mL aliquot of the washed Au NPs was then added to a 16 mL glass vial with a magnetic stir bar. To this solution, we added 100 μL of 1.0 M NaOH to raise the pH of the growth solution to pH ~10, followed by the addition of 20 μL of tetraethoxysilane (TEOS) under rapid magnetic stirring. The addition of TEOS was repeated *x* times (where *x* = 1—8) in 60 min intervals to achieve a final SiO_2 shell thickness from 5 nm to 22 nm.

Materials Characterization

Scanning electron microscopy (SEM) analysis of the Cu_2O NWs was conducted on an FEI Nova Nano 430 SEM operated at 15 kV and located at the Nanoscale Research Facility (NRF) at the University of Florida (UF). X-ray diffraction (XRD) patterns of the Cu_2O NWs on the FTO glass substrate were obtained using an X'Pert powder diffractometer (PANalytical Systems) with Cu Kα radiation (λ = 1.5406 Å) located at the Major Analytical Instrumentation Center (MAIC) at UF. Raman spectroscopy was performed using a Horiba Aramis Raman instrument, also housed at NRF at UF using a 532 nm laser excitation wavelength. X-ray photoelectron spectroscopy (XPS) analysis of the Cu_2O NWs was conducted at MAIC using a PHI 5000 *VersaProbe* II XPS instrument with a focused monochromatic Al Kα X-ray (1486.6 eV) source and a spherical section analyzer. A 50 W X-

ray beam was focused to a 200 μm diameter spot size and incident normal to the sample with the photoelectron detector at 45° off-normal. Adventitious carbon (C) was used as a binding energy reference at 284.8 eV to correct for any specimen charging effect for all XPS spectra. To prepare the Cu_2O NWs for structural analysis by transmission electron microscopy (TEM), the NWs were subjected to brief sonication for 20 s to disperse the NWs in solution. TEM samples were then prepared by dropping 6 μL of the Cu_2O NW suspension onto a Holey Carbon 400 mesh Cu grid (Ted Pella, Inc.) and drying in ambient air. TEM analysis was then performed using a JEOL 200CX TEM operated at 200 kV and high-resolution transmission electron microscopy (HRTEM) was performed on a JEOL 2010F HRTEM. Both TEM instruments are located at MAIC (UF). Advanced materials characterization was carried out at the Center for Functional Nanomaterials at Brookhaven National Laboratory (BNL), Upton, NY. Additional HRTEM images of Cu_2O NWs were acquired using a JEOL 2100F HRTEM operated at 200 kV. Annular dark-field scanning transmission electron microscopy (ADF-STEM) imaging of Cu_2O NWs was conducted on a Cs-corrected Hitachi HD-2700C equipped with a Cold-FEG operated at 200 kV. Images were acquired using a probe convergence angle of 23 mrad and the inner collection angle of the ADF detector was 53 mrad. Electron Energy Loss Spectroscopy (EELS) mapping of the Cu_2O NWs was obtained using a Gatan Enfina spectrometer. The collection angle was set to 20 mrad and dispersions of 1.25 eV/ch or 0.3 eV/ch were used.

Photocathode Device Preparation

Photocathodes were prepared by drop-casting the previously prepared Cu_2O NW and $Au@SiO_2$ NP solutions onto clean FTO glass substrates. The FTO substrates were first cleaned via ultrasonication for 1 h in a solution of 1:1:1 (by volume) Nanopure© H_2O:2-propanol:acetone. The substrates were then copiously rinsed with Nanopure© H_2O, and then dried with a stream of compressed air. Photocathodes were then prepared by drop-casting aliquots of the nanoparticle suspensions directly onto the clean FTO glass substrates.

Variability in device construction was minimized by using a single "master" solution of Cu_2O NWs at a fixed concentration for the preparation of all photocathodes. This preparation method enabled remarkable photoelectrochemical reproducibility between photocathodes, with ca. 5% variability observed between devices. This fabrication process also provided a simple method of controlling the Cu_2O film thickness (1—5 μm) by varying the total volume of solution that was drop-cast onto the FTO substrate. All plasmonic devices (Cu_2O/Au@SiO_2) were prepared in triplicate from the same master Cu_2O NW solution used for control devices with a "master" Au@SiO_2 NP solution used for each different SiO_2 shell thickness investigated. This preparation method reduced device variability (ca. 5%). Prior to all photoelectrochemical experiments, the photocathodes were subjected to a mild heat treatment at 120 °C for 30 min to improve the adhesion between the NWs and the FTO glass substrate.

Photoelectrochemical Characterization

The photoelectrochemical characteristics of these materials were investigated via the construction of a three-electrode electrochemical cell controlled by a potentiostat (EC Epsilon, Bioanalytical Systems, Inc.). The Cu_2O NW photocathode served as the working electrode, with a Ag/AgCl (saturated KCl) reference electrode and a platinum (Pt) wire auxiliary electrode all immersed in 0.10 M Na_2SO_4 (pH 6) as the supporting electrolyte. All potentials are reported relative to the Reversible Hydrogen Electrode (RHE), which represents the potential of the Standard Hydrogen Electrode (SHE) adjusted for the pH of the solution with the following equation:[4]

$$E_{RHE} = E_{Ag/AgCl} + 0.059\left(pH\right) + E^{\circ}_{Ag/AgCl}$$

where E_{RHE} is the converted potential vs. RHE, $E_{Ag/AgCl}$ is the experimental potential measured relative to the Ag/AgCl reference electrode, and $E^{\circ}_{Ag/AgCl}$ is the standard potential of the Ag/AgCl reference electrode relative to the RHE at 25 °C (0.1976 V_{RHE}).[4] All

photoelectrochemical experiments were repeated in triplicate on three independently fabricated photocathodes. Photocathodes were illuminated through the FTO glass substrate with simulated sunlight using an ozone-free 300 W Xe lamp (Newport Corp.) equipped with an air mass (AM) 1.5G filter (Newport Corp.). It should be noted that all measurements were conducted at an incident power of $I_0 = 100 \pm 10$ mW/cm^2 (1-sun intensity) unless indicated otherwise. The influence of applied bias on device photocurrent [$J_{ph}(E)$] was assessed under both steady-state light and dark conditions [$J_{ph}(E) = J_{light}(E) - J_{dark}(E)$] while a particular applied bias ($E_{appl} = -0.50$—1.4 V_{RHE}) was maintained by the potentiostat to exclude the influence of scan rate on device J_{ph}. Controlled potential electrolysis [$J_{ph}(t)$] and power-dependent photocurrent [$J_{ph}(I_0)$] experiments were conducted using the three-electrode configuration mentioned above while the photocathodes were poised at $E_{appl} = 0$ V_{RHE}. Incident photon-to-charge conversion efficiency (IPCE) measurements were conducted using a set of band pass filters (λ = 400-700 nm) with a bandwidth of $\Delta\lambda = 20$ nm ± 10 nm (Thor Labs, Inc.) coupled with an AM 1.5G optical filter. The measured J_{ph} at each irradiation wavelength was then converted into an IPCE value according to the following equation:[5]

$$IPCE(\%) = \frac{(J_{ph} \times 1240)}{(I_0 \times \lambda)} \times 100$$

where J_{ph} is the measured photocurrent density (in mA cm^{-2}), I_0 is the power density of light incident upon the device (mW cm^{-2}), λ is the wavelength of incident light (nm), and the value 1240 is a conversion factor between photon energies expressed in eV and wavelength (in nm).

Photoluminescence (PL) Studies

Photoluminescence (PL) measurements were carried out using a Horiba Aramis Raman system, which is a software-selectable multi-wavelength Raman/PL system located at NRF (UF). The PL spectra were collected by using a 532 nm laser with a grating of 1800 g/mm to simultaneously excite the band gap transitions of the Cu_2O NWs and the LSPR of the Au NPs. The samples were focused using a 100x objective lens. The laser spot size used for

each measurement was ca. 5 μm in diameter with an incident power of 0.6 mW and an acquisition time of 5 s. PL spectra were acquired on pristine Cu_2O-only and Cu_2O/Au@SiO_2 devices prior to photoelectrochemical measurements. All PL measurements were acquired from at least 9 different spots selected at random on each device. All PL emission spectra were then averaged to mitigate any signal variability associated with irregularities in film composition. Furthermore, each device condition investigated (control or plasmonic) was examined in duplicate to further ensure accurate representation of the PL enhancement factor for the various devices.

Discrete Dipole Approximation (DDA) Simulations

The program DDSCAT v7.1 developed by Draine and Flatau was used for all calculations.[6,7] The wavelength-dependent extinction, scattering, and absorption cross sections were calculated for each Au@SiO_2 geometry, and electromagnetic field distributions were visualized around each particle under 525 nm light irradiation. The dielectric functions for Au and SiO_2 were taken from ref. 8 and ref. 9, respectively. The core@shell morphology was modeled by two concentric spheres immersed in a pure water medium with refractive index, n = 1.333. For all simulations, light propagated in the x-direction and was polarized in the y-direction. OriginLab, a scientific graphing and data analysis software package, was used to plot the raw data and visualize the EM field distribution around a single nanoparticle.

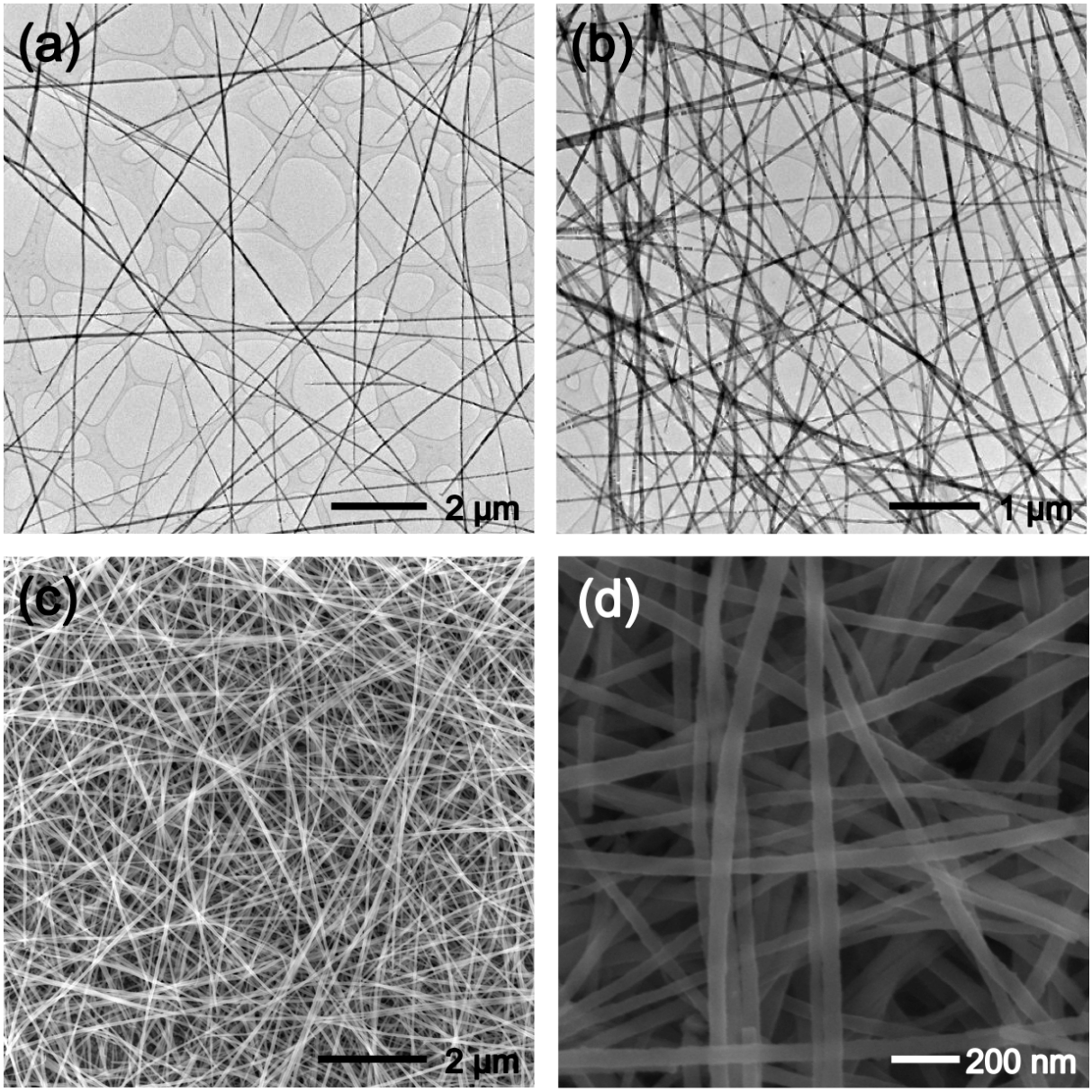

Figure S1. Morphology and Physical Dimensions of Cu_2O Nanowires
Inspection of the nanowires by **(a,b)** TEM and **(c,d)** SEM while on TEM grids and FTO glass substrates, respectively. Although some nanowires exhibit shorter lengths due to damage during sample preparation, a cursory inspection of the TEM images (a-c) reveals that the majority of these nanowires display diameters (d) of 80 ± 10 nm and typical lengths (l) of 10—25 µm. The tendency for these high-aspect ratio (l/d ~100—300) nanowires to form interwoven nanowire networks upon drying of the substrate is also apparent (a,b). This propensity for forming intertwined nanowire mats over a large area is more clearly shown by the SEM images (c,d).

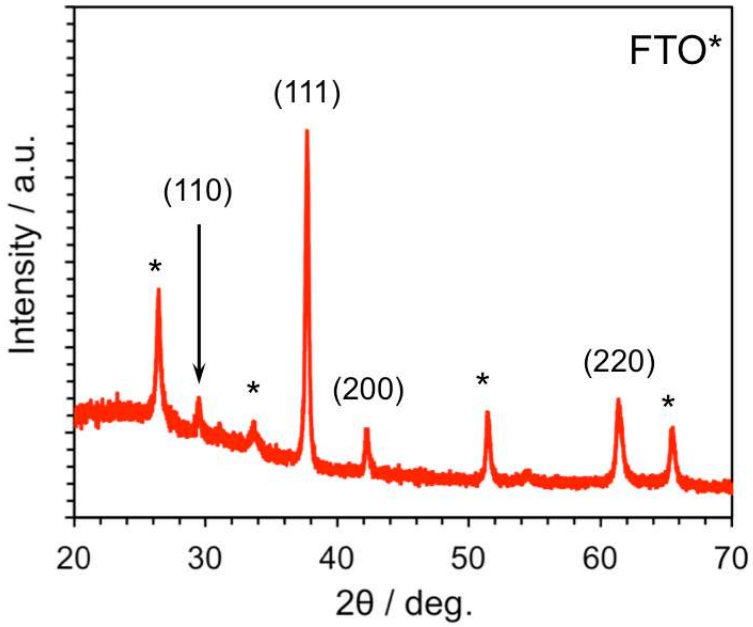

Figure S2. X-ray Diffraction (XRD) Pattern of Cu_2O Nanowires
XRD was used to evaluate the crystallinity of these nanowires after deposition onto the FTO glass substrate. The peaks are indicative of the Cu_2O phase and labeled accordingly.[1,10,11] No signs of metallic Cu or CuO phases were observed in the XRD pattern from these nanowires, indicating that these materials are composed of the Cu_2O phase. The peaks marked by an asterisk (*) denote those features from the underlying FTO substrate itself.

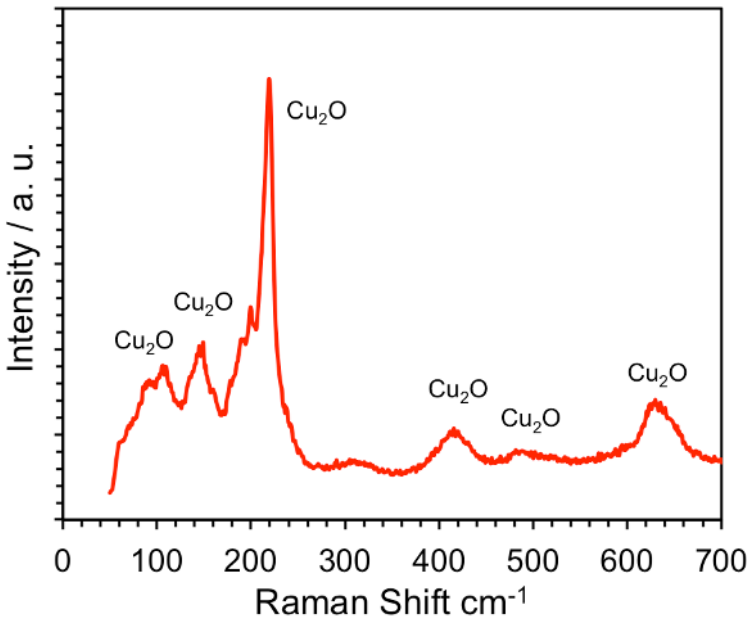

Figure S3. Raman Spectroscopy of Cu_2O Nanowires
Raman spectroscopy was used to evaluate the phase of these nanowires on FTO glass substrates. The Raman features observed are indicative of the Cu_2O phase.[12,13] A signal may exist at ca. 300 cm^{-1} that could be indicative of a small CuO phase due to slight surface oxidation of the nanowires. In general, however, the Raman spectra of these nanowires demonstrates that they are chiefly composed of the Cu_2O phase.

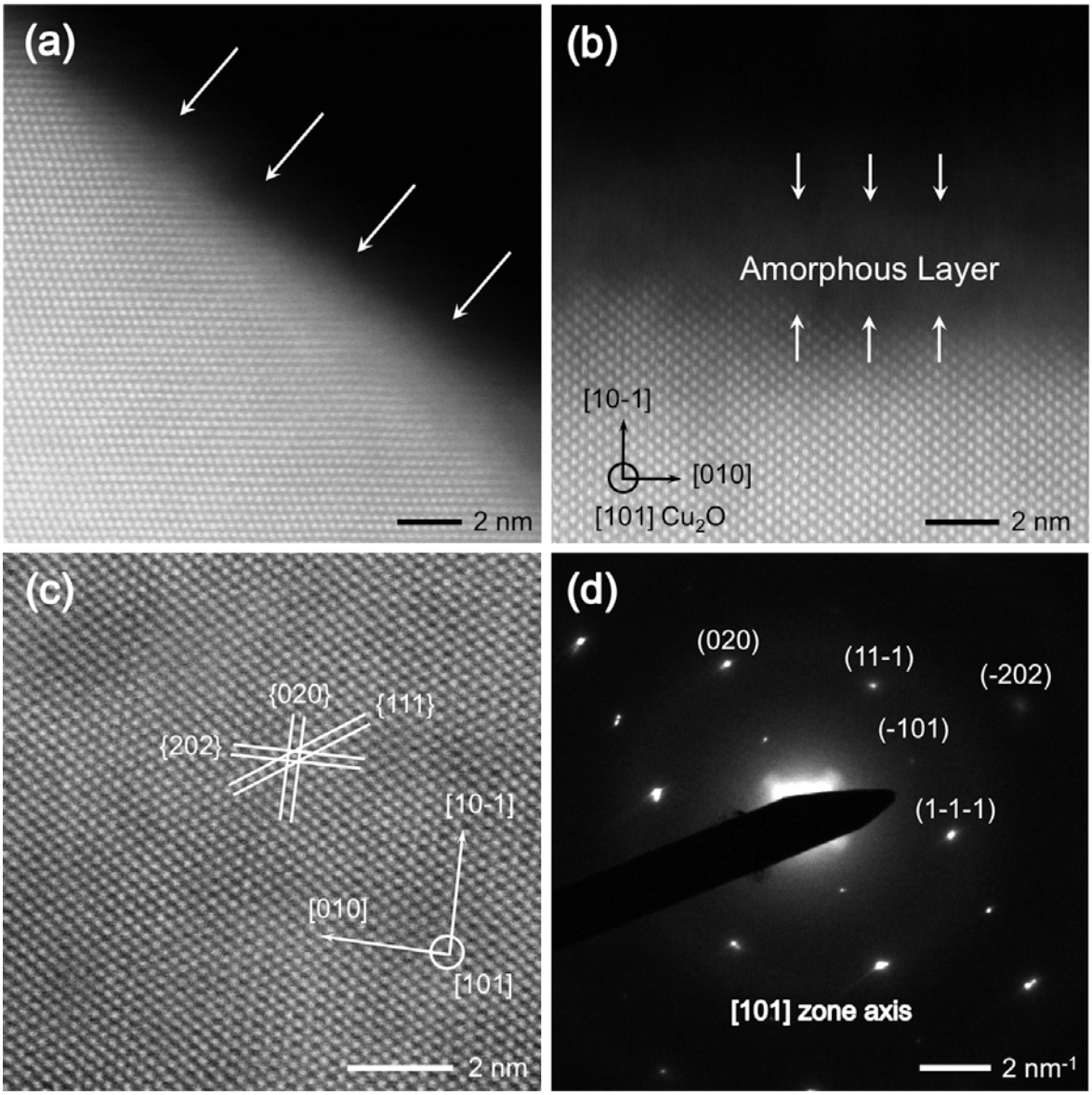

Figure S4. Structural Characterization of Cu_2O Nanowires
(a-c) Annular dark-field scanning transmission electron microscopy (ADF-STEM) images of an individual Cu_2O nanowire with crystal planes indexed to those of the Cu_2O phase. White arrows in (a,b) highlight the amorphous layer that runs along the length of the nanowire surface. **(d)** Selected area electron diffraction (SAED) pattern along the [101] zone axis from the nanowire shown in (c) with reflections indexed to those of the Cu_2O phase.

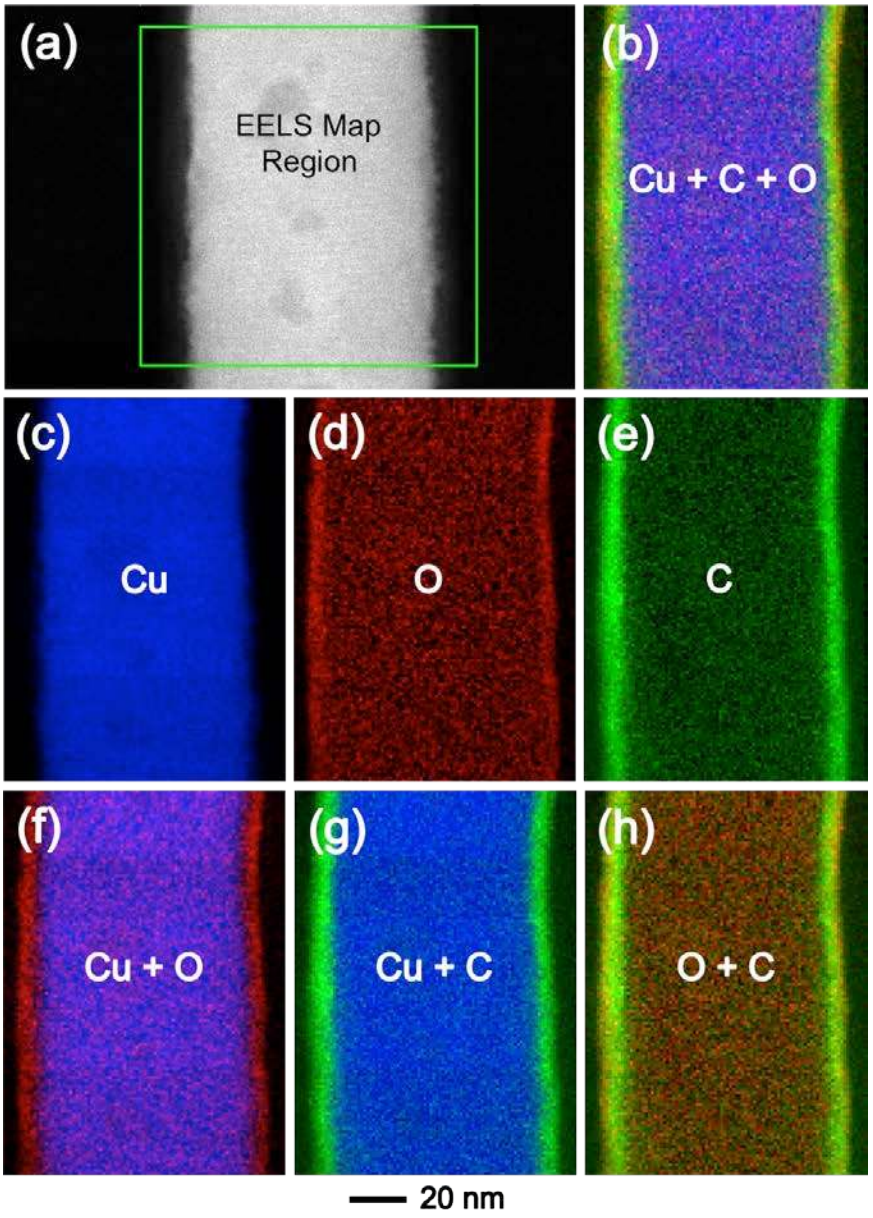

Figure S5. Electron Energy Loss Spectroscopy (EELS) Mapping of Nanowires
Investigation of the chemical composition of these nanowires by **(a)** ADF-STEM imaging and **(b-h)** EELS mapping of the elemental distribution of copper (Cu, blue), oxygen (O, red), and carbon (C, green) in a single Cu_2O nanowire. **(a)** ADF-STEM image shows the actual Cu_2O nanowire investigated by EELS. The EELS maps (b-h) depict: **(b)** convolution of all three Cu, O, and C signals, **(c)** Cu-only signals, **(d)** O-only signals, **(e)** C-only signals, **(f)** convolution of Cu and O signals, **(g)** convolution of Cu and C signals, and **(h)** convolution of O and C signals. From these maps it is clear that a C/O layer persists along the length of the Cu_2O nanowires, which we assign to that of glucose present in the initial nanowire synthesis. The 20 nm scale bar at the bottom of the figure applies to all images (a-h).

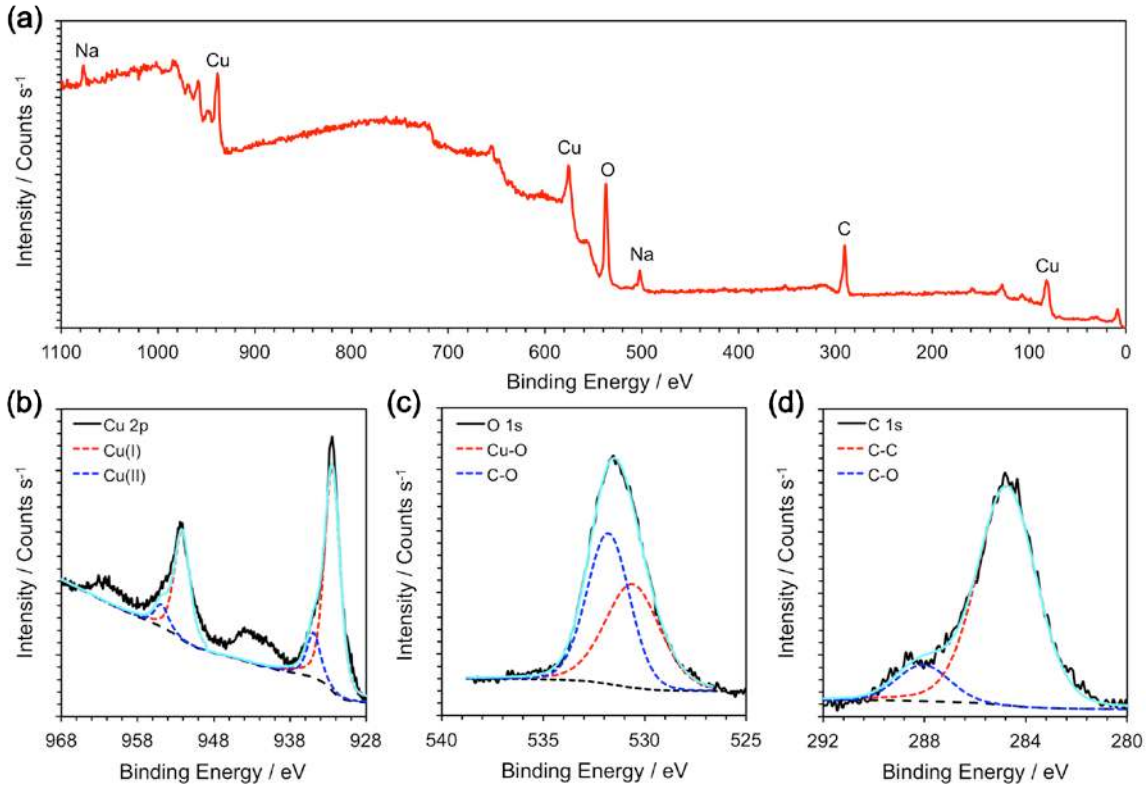

Figure S6. X-ray Photoelectron Spectroscopy (XPS) of Cu_2O Nanowires
XPS analysis of the oxidation state and chemical composition of the nanowires. **(a)** Full scan XPS spectrum of Cu_2O nanowires with corresponding narrow scan XPS spectra of **(b)** Cu 2p, **(c)** O 1s, and **(d)** C 1s regions. The narrow scan XPS spectrum from the Cu 2p region (b) showed binding energies of 932.8 eV and 952.6 eV for the Cu 2p 3/2 and Cu 2p 1/2, respectively, consistent with prior reports for Cu_2O materials.[10,11] It is well known that CuO is easily distinguished from Cu_2O by the "shake-up" satellite peaks at higher binding energies relative to the main Cu 2p 3/2 and Cu 2p 1/2 peaks in CuO.[10,11] A very slight shoulder is observed off the main Cu 2p peaks and the presence of small features between 938-948 eV and 958-968 eV in our spectra suggests slight surface oxidation of the wires, but confirms Cu_2O as the dominant phase.[10,11] The O 1s region (c) shows a broad feature centered at 531 eV with a discernable shoulder at lower binding energies. Deconvolution of this main feature suggests a contribution from the O atoms in the Cu_2O lattice itself (530.8 eV) and those O atoms bound to C (532.1 eV), likely from the glucose species.[10] The C 1s region (d) shows a main peak from adventitious C at 284.8 eV, but also revealed the presence of a significant shoulder at higher binding energy. Deconvolution of this main peak into its components showed this shoulder could be fit by another peak centered around 288.4 eV. This feature is very similar to that previously reported for C-coated Cu_2O nanowires,[10] and we therefore attribute these C/O species to that of glucose.

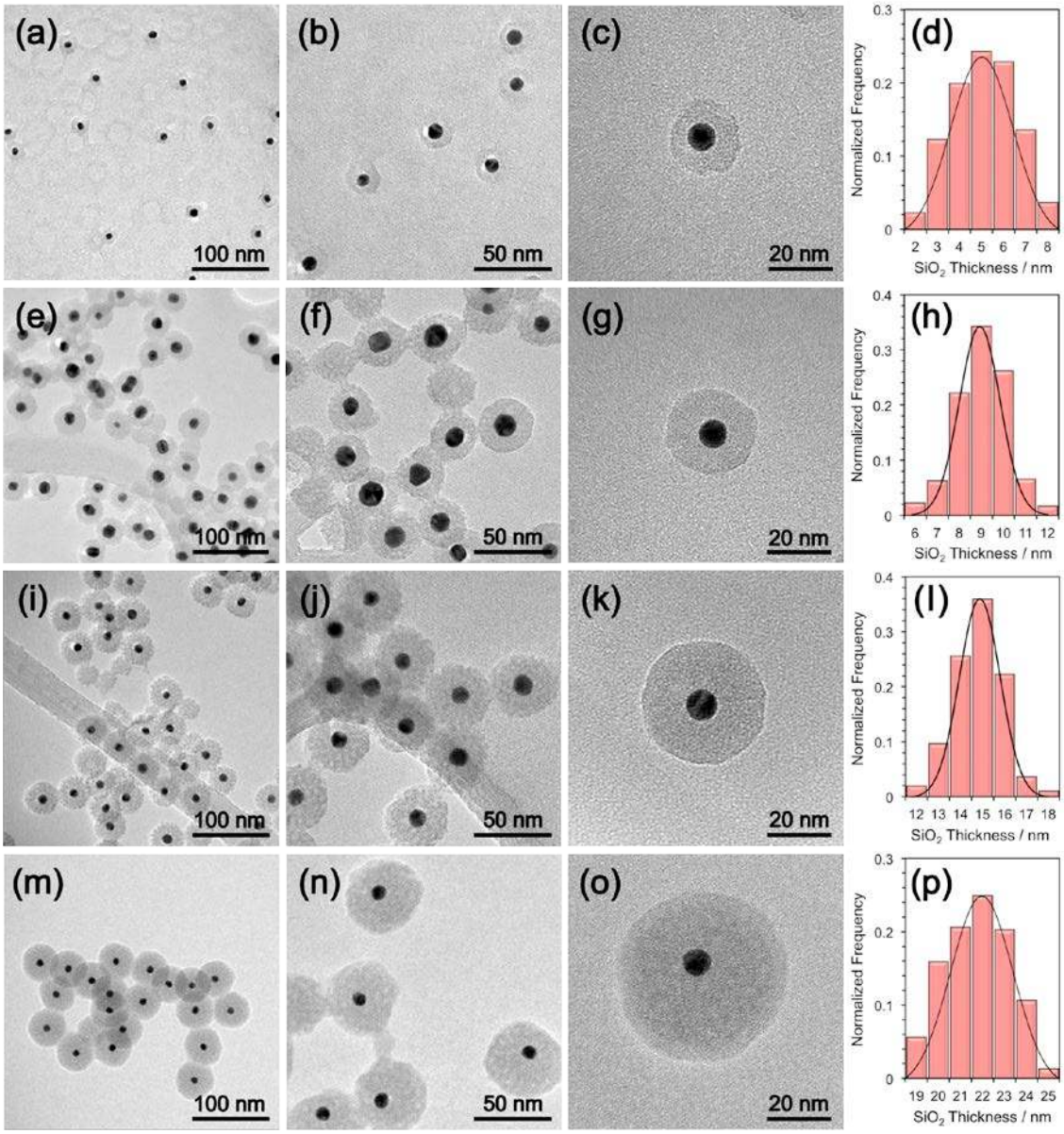

Figure S7. Size Distributions of Au@SiO_2 Nanoparticles
TEM images and corresponding size-distribution histograms for 10 nm Au nanoparticles encapsulated by SiO_2 shells of various thicknesses: **(a-d)** 5 ± 2 nm, **(e-h)** 9 ± 1 nm, **(i-l)** 15 ± 1 nm, and **(m-p)** 22 ± 2 nm SiO_2 shells. Over 200 nanoparticles were counted for each of the four different Au@SiO_2 samples to construct the size distribution histograms.

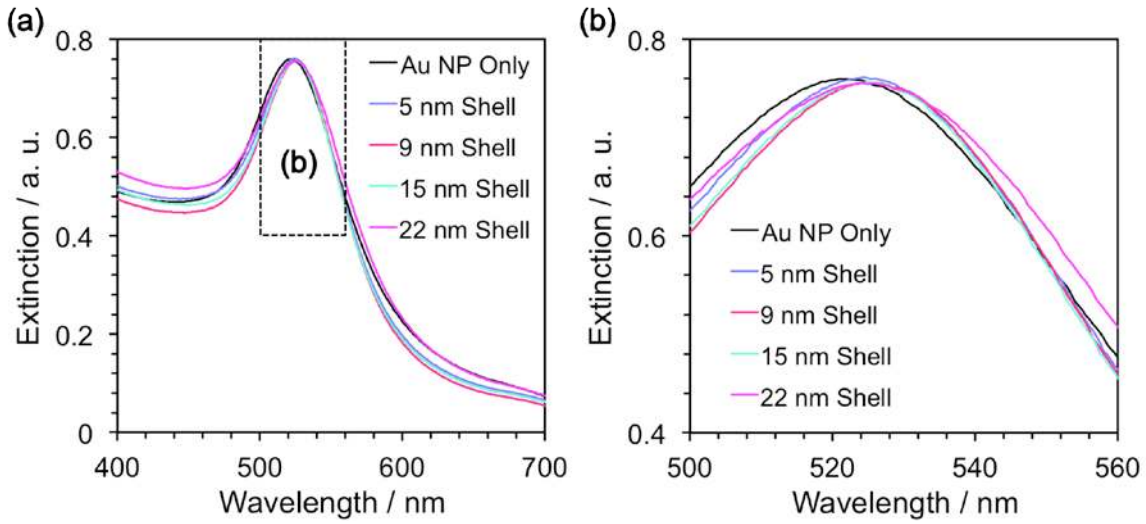

Figure S8. Optical Properties of Au@SiO_2 Nanoparticles
(a) Ultraviolet (UV)-Visible extinction spectra of Au@SiO_2 nanoparticles with a 10 nm Au nanoparticle core encapsulated by different thicknesses of SiO_2 shells: 5 ± 2 nm, 9 ± 1 nm, 15 ± 1 nm, and 22 ± 2 nm SiO_2 shells. **(b)** A slight red shift in LSPR peak maximum (λ_{max}) was observed upon deposition of the SiO_2 shell, shifting from 521 nm for uncoated Au nanoparticles to 525 nm for Au@SiO_2 nanoparticles. However, after the initial change in λ_{max}, no significant shift was observed (Figure S8b). We do note a slight increase in extinction occurring at shorter (λ < 460 nm) and longer (λ > 600 nm) wavelengths for the thickest SiO_2 shells (22 ± 2 nm).

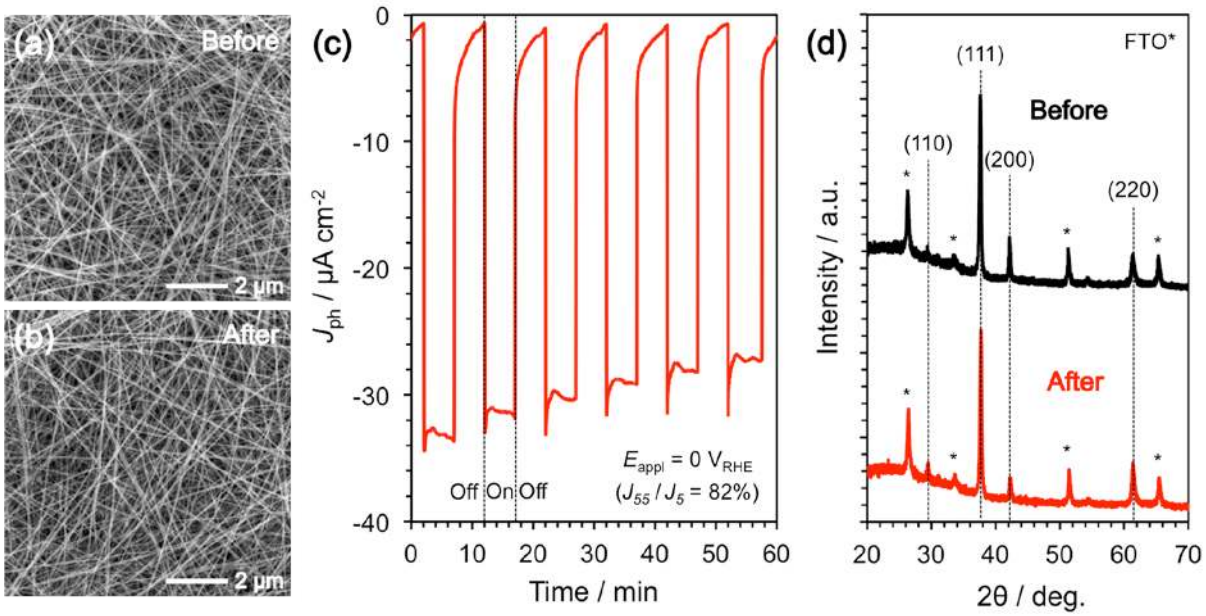

Figure S9. Extended Photoelectrochemical Stability of Cu_2O Photocathodes
The control (Cu_2O-only) photocathodes were evaluated for an extended 1 h period, rather than the shorter 20 min period usually employed for evaluation of Cu_2O photocathodes.[10] SEM images of the device were acquired before **(a)** and after **(b)** 1 h of photoelectrohcemical testing. **(c)** Controlled potential electrolysis of a Cu_2O photocathode at 0 V_{RHE} under periodic (5 min on/off) AM 1.5G irradiation (300 ± 25 mW/cm^2). The stability of the device was evaluated by comparing the J_{ph} at 5 min (J_5) to that observed at 55 min (J_{55}), which showed that ca. 82% of the initial J_{ph} was retained after the 1 h irradiation period. This value is very similar to that previously reported for Cu_2O photocathodes employing C-based coatings (80%),[10] further supporting the viability of this approach for stabilizing Cu_2O materials. **(d)** X-ray diffraction pattern of Cu_2O photocathodes before (black curve) and after (red curve) 1 h of controlled potential electrolysis. All the original peaks are retained and no new peaks due to metallic $Cu^{(0)}$ or CuO were observed, indicating the stability of these Cu_2O nanowires. The peaks marked by an asterisk (*) denote those features from the underlying FTO substrate.

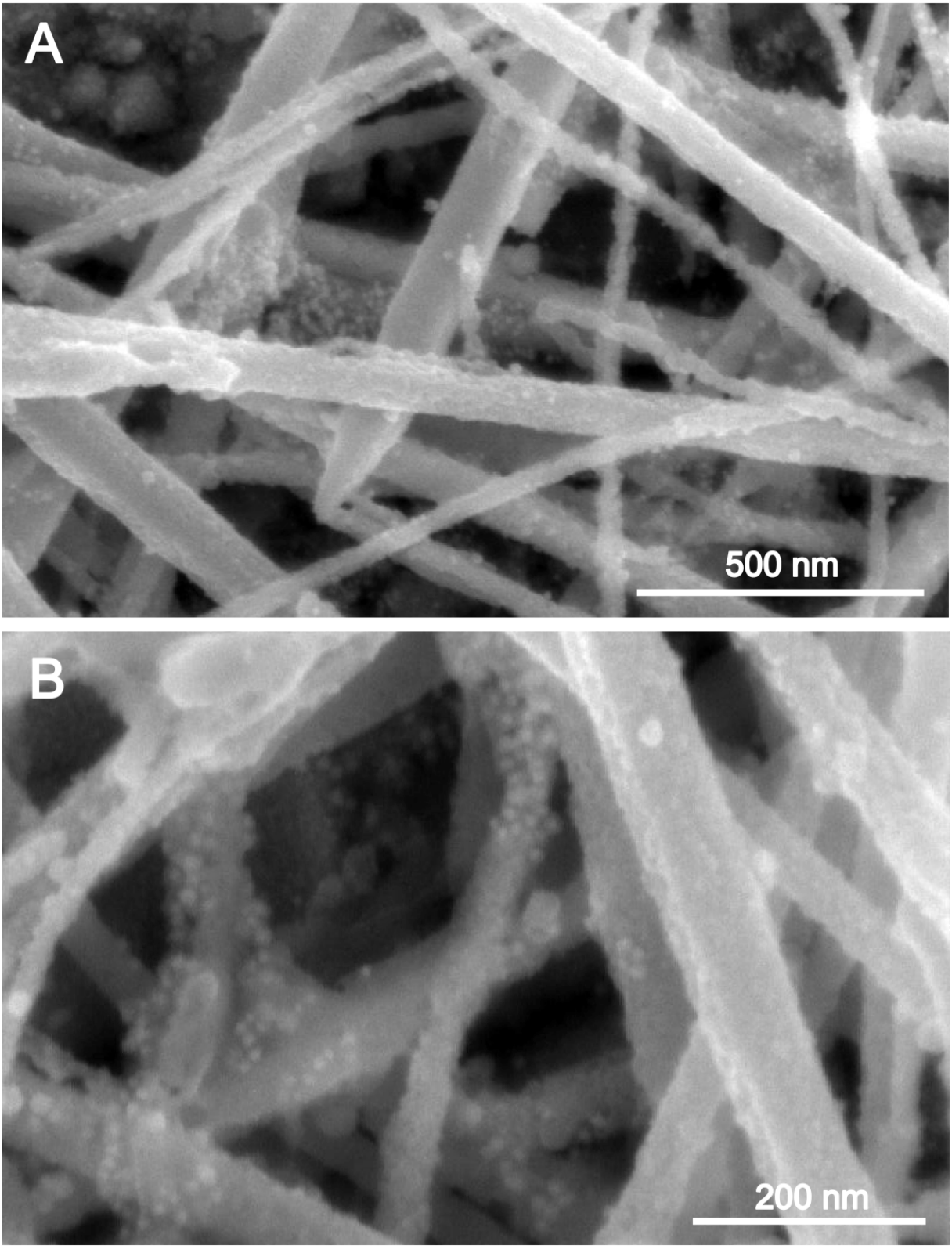

Figure S10. Distribution of Au@SiO_2 Nanoparticles within Plasmonic Photocathodes
SEM images of plasmonic Cu_2O/Au@SiO_2 photocathodes showing the distribution of Au@SiO_2 nanoparticles encapsulated by a 5 ± 1 nm SiO_2 shell. These images show that the drop-casting methods used for plasmonic photocathode fabrication provide a roughly homogeneous distribution of Au@SiO_2 nanoparticles embedded on and within the Cu_2O nanowire network.

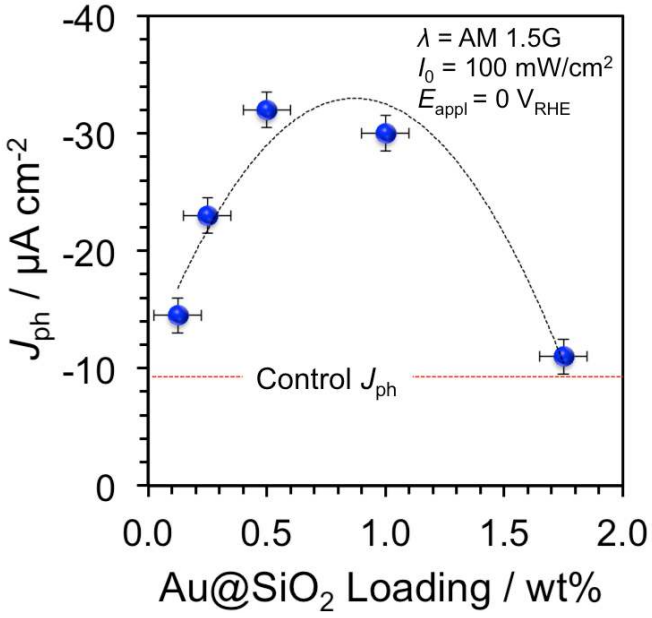

Figure S11. Influence of Au@SiO_2 Loading on Photocathode Performance
The optimal Au@SiO_2 nanoparticle loading was first investigated to determine a suitable ratio between the plasmonic metal and semiconductor components for achieving the maximum photocurrent (J_{ph}) from the plasmonic device. The initial addition of Au@SiO_2 nanoparticles induces a monotonic increase in J_{ph} at 0 V_{RHE} until 0.5 ± 0.1 wt%, at which point a plateau is reached up to ~1.0 ± 0.1 wt% before a rapid decline in device performance was observed with further loading at 1.8 ± 0.1 wt%. We attribute this reduction at increased Au@SiO_2 nanoparticle loading to photonic competition between Au nanoparticles and Cu_2O nanowires for incident light, as both components absorb similar regions of the solar spectrum (Figure 2). This observation is also consistent with a recent theoretical model developed to interpret this empirical phenomenon, which is based on the changing spatial location of the enhanced near-fields within the device as a function of metal nanoparticle loading.[14] The optimized Au@SiO_2 loading of 0.5 ± 0.1 wt% was adopted for all subsequent photoelectrochemical experiments.

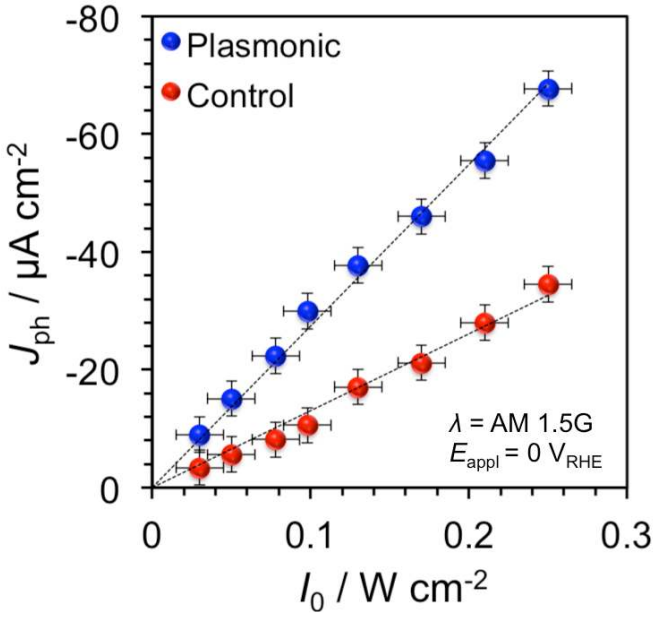

Figure S12. Influence of Incident Light Power on Photocathode Performance
The control (Cu_2O-only) photocathode (red) and the plasmonic (Cu_2O/Au@SiO_2) photocathode (blue) both show a linear dependence on incident light power (I_0) while poised at 0 V_{RHE} and irradiated with AM 1.5G light. These data show that the plasmonic device produces more photocurrent (J_{ph}) at any incident power, suggesting that the plasmonic device harvests light better than the control.

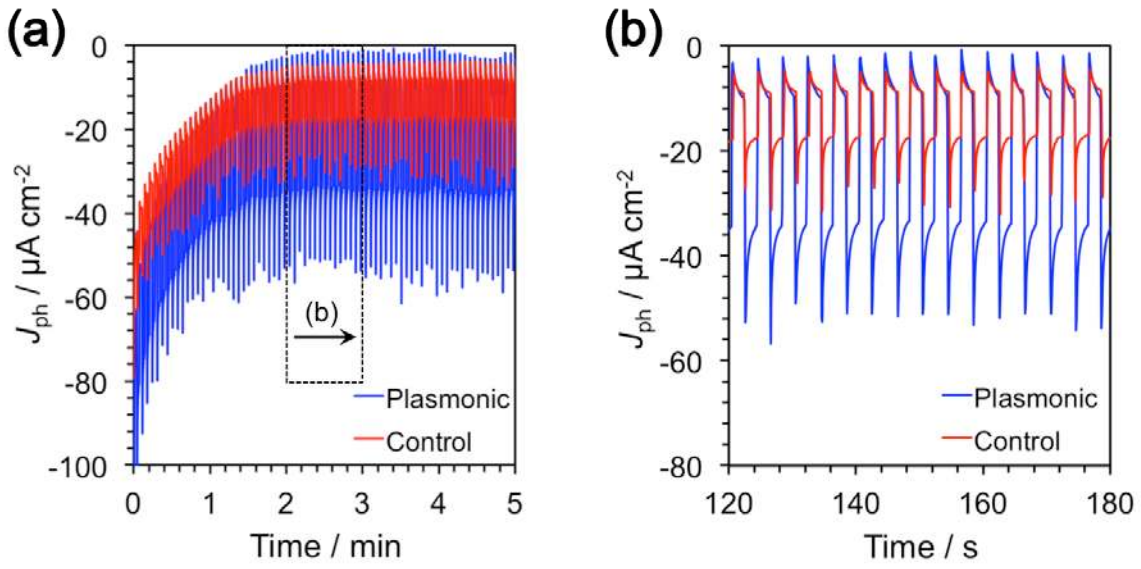

Figure S13. Comparison of Plasmonic and Control Photocathodes
(a) The control (Cu_2O-only) photocathode (red) and the plasmonic (Cu_2O/Au@SiO_2) photocathode (blue) show a marked difference in photocurrent (J_{ph}) under periodic (2 s on/off) 1-sun (I_0 = 100 mW cm^{-2}) AM 1.5G light while poised at E_{appl} = 0 V_{RHE}. A prompt and reproducible J_{ph} response was observed form both devices over sustained periods, further indicating device stability. **(b)** A closer inspection of these data over the given period from 120—180 s shows that the plasmonic device produces ca. 3 times more photocurrent (J_{ph} = −29 ± 1 μA cm^{-2}) under simulated solar conditions than the control (J_{ph} = −9 ± 1 μA cm^{-2}).

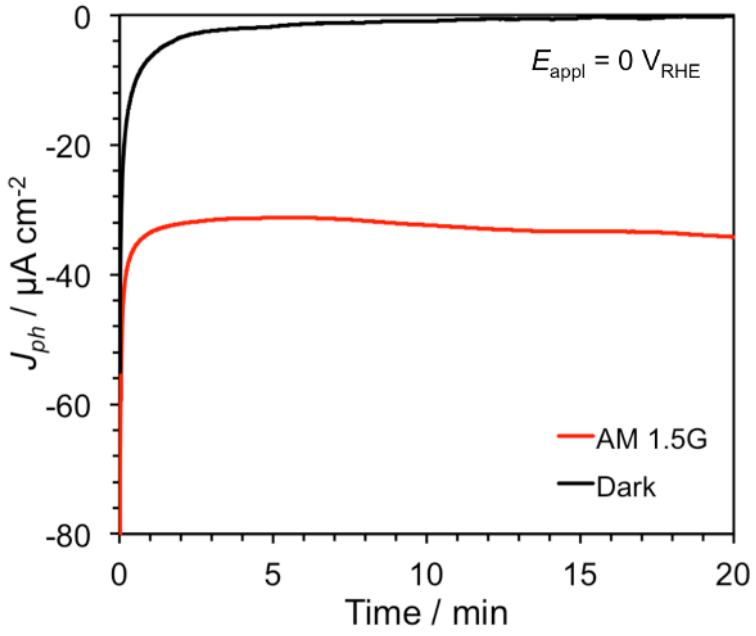

Figure S14. Photoelectrochemical Stability of Plasmonic Photocathodes
The photoelectrochemical stability of the plasmonic photocathode was investigated in a similar manner to that employed for the control device. The plasmonic photocathode was first poised at 0 V_{RHE} for 20 min in the dark (black curve) to determine the stability of these materials under the influence of the applied bias itself (E_{appl} = 0 V_{RHE}) while in the dark. The experiment was then repeated at the same potential (0 V_{RHE}) under AM 1.5G irradiation at 100 ± 10 mW/cm^2 for another 20 min (red curve). A steady-state J_{ph} was achieved after ~2 min and maintained over the 20 min irradiation period without any sign of electrochemical degradation.

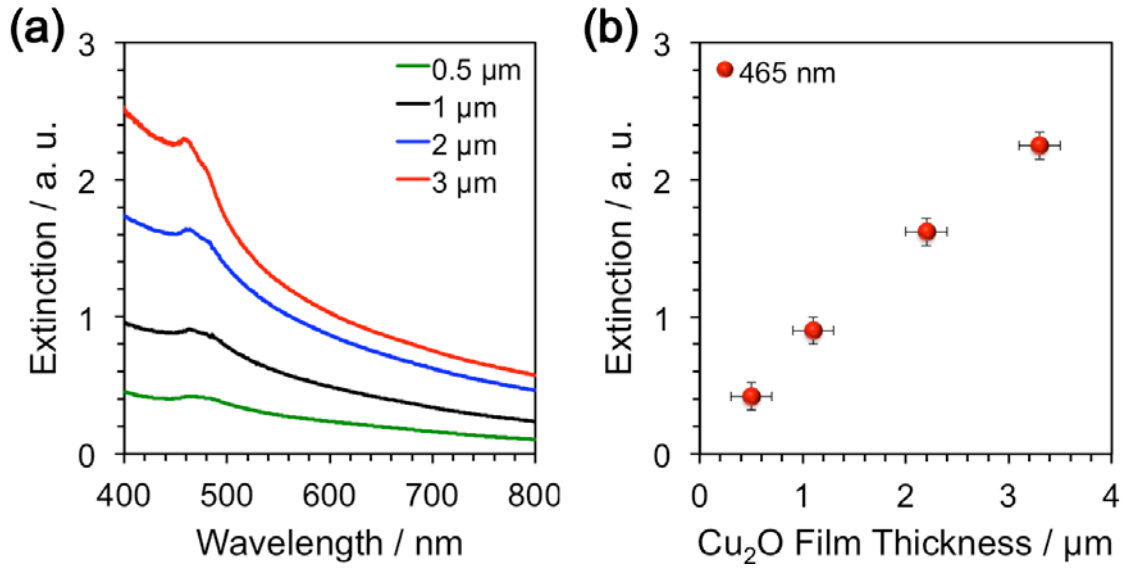

Figure S15. Influence of Cu_2O Loading on Optical Properties of Control Devices
(a) Extinction spectra of Cu_2O-only photocathodes of varying semiconductor film thickness from 0.5 ± 0.2 µm to 3 ± 0.2 µm. **(b)** The extinction at 465 nm was extracted from the curves shown in (a) and plotted as a function of film thickness to reveal a roughly linear increase in extinction with increasing semiconductor film thickness. These data clearly indicate that increasing the Cu_2O film thickness increases the optical density of the photocathode.

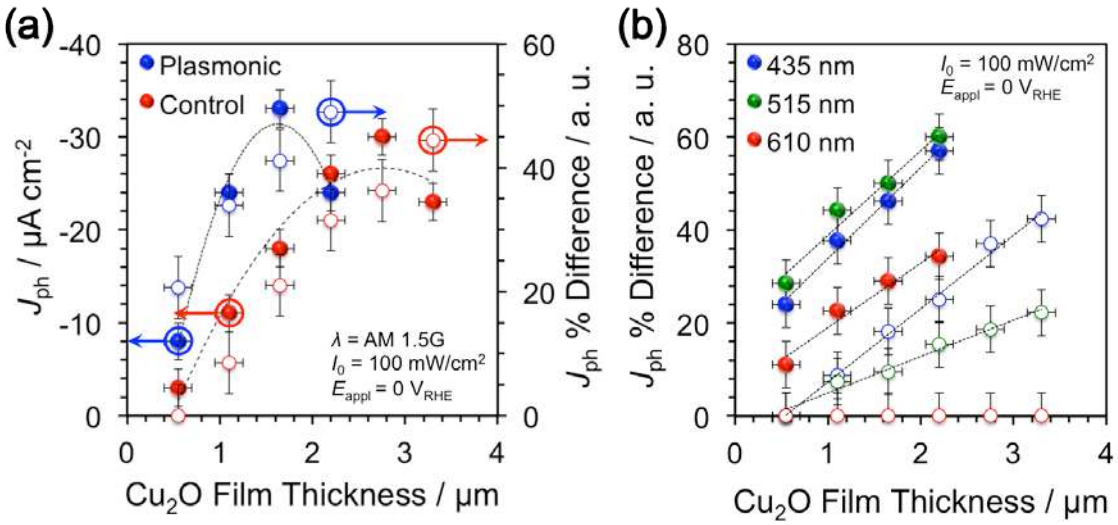

Figure S16. Influence of Cu_2O Loading on Photocathode Performance
(a) Photocurrent (J_{ph}) produced from plasmonic (filled blue points) and control (filled red points) devices as a function of Cu_2O film thickness plotted on the left ordinate axis. The J_{ph} % difference between frontside and backside illumination directions for the plasmonic (open blue points) and the control (open red points) devices as a function of Cu_2O film thickness are plotted on the right ordinate axis. Frontside illumination is defined as irradiation through the Cu_2O film while backside illumination is defined as irradiation through the FTO glass substrate. After conducting measurements under both device orientations, the J_{ph} difference [$\Delta J_{ph} = J_{ph}$(backside) − J_{ph}(frontside)] was computed and then used to calculate the J_{ph} % difference under AM 1.5G irradiation. **(b)** The J_{ph} % difference produced by the plasmonic device (filled points) and the control device (open points) as a function of Cu_2O film thickness under different irradiation wavelengths: λ > 435 nm (blue), λ > 515 nm (green), and λ > 610 nm (red).

Interpretation of photoelectrochemical data presented in Figure S15.

Although increasing the Cu_2O film thickness increases the optical density of the semiconductor film (Figure S14), it also extends the diffusion distance for excited-state charge carriers within the nanowire network. Consequently, a J_{ph} maximum is often observed with respect to semiconductor film thickness. This maximum occurs when the optimal balance between light absorption and charge carrier extraction has been achieved. These data in Figure S15a show that a J_{ph} maximum occurred for a Cu_2O film thickness of ca. 2.8 μm in the control device (filled red points), which is consistent with the reported light absorption depth (α^{-1}) for Cu_2O at the band edge (α^{-1}(600 nm) = 2.2 μm).[15] The incorporation of Au@SiO_2 nanoparticles into the Cu_2O nanowire network substantially shifted the J_{ph} maximum of the plasmonic device to lower Cu_2O loadings (~1.6 μm), eliminating the need for ca. 40% of the semiconductor in the plasmonic device (Fig. S15a, filled blue points).

It has previously been shown that frontside illumination generates the majority of electron-hole (*e*-*h*) pairs farther away from the FTO back contact compared to backside illumination.[16,17] As a result, this condition increases the average diffusion distance for the majority carriers (h^+) and subsequently hinders the charge collection efficiency within the nanowire network. We therefore expected that the J_{ph} obtained during frontside illumination would be diminished more significantly as the semiconductor film thickness was increased, because the thicker devices would more effectively absorb incident light. This phenomenon was quantified by comparing the J_{ph} % difference between illumination directions, as plotted on the right ordinate axis in Fig. S15a (open points). Indeed, the J_{ph} % difference became more pronounced with increasing Cu_2O film thickness in the control device (open red points).

This phenomenon was further exacerbated by the incorporation of the $Au@SiO_2$ nanoparticles, as we observed a steeper increase in J_{ph} % difference for the plasmonic device as compared to the control as a function of Cu_2O film thickness (open blue points). These results strongly suggest that the device enhancements provided by the plasmonic nanoparticles originate from increased light-harvesting efficiency within the photoactive Cu_2O layer.

To further investigate the nature of this light-harvesting enhancement and correlate it with the optical properties of the $Au@SiO_2$ nanoparticles, additional photoelectrochemical experiments were conducted under various excitation conditions, as shown in Figure S15b. In general, these data show that as the Cu_2O film becomes thicker, it absorbs all wavelengths of incident light more proficiently, increasing the overall J_{ph} % difference for both plasmonic (filled points) and control (open points) devices. Since the light absorption depth (α^{-1}) for Cu_2O varies as a function of wavelength (α^{-1}(620 nm) = 5.2 μm; α^{-1}(500 nm) = 0.8 μm),[15] it is expected that these distinct wavelength ranges should show different dependencies on the Cu_2O film thickness. Indeed, by taking the slope of these curves to indicate the extent to which incident light is absorbed by the semiconductor film, a substantial discrepancy in light absorption is observed across different wavelengths (compare slope of open blue points to open green points). In contrast, the slopes of the λ > 435 nm curve (filled blue points) and λ > 515 nm curve (filled green points) for the plasmonic device are nearly identical, indicating a substantial increase in extinction for λ > 515 nm wavelengths. This represents a substantial increase in utilization of incident light for the plasmonic device as compared to the control. Interestingly, although the slope of the λ > 435 nm curves don't significantly differ between plasmonic (filled blue points) and control (open blue points), the entire curve has been shifted upward with respect to Cu_2O film thickness. This substantial shift in J_{ph} % difference further indicates an overall improvement in light absorption at most visible-light wavelengths for the plasmonic device as compared to the control. Finally, it is noted that even λ > 610 nm are attenuated within the plasmonic device with increasing Cu_2O film thickness, whereas the control device registers no difference in light absorption at these longer wavelengths regardless of the Cu_2O film thickness.

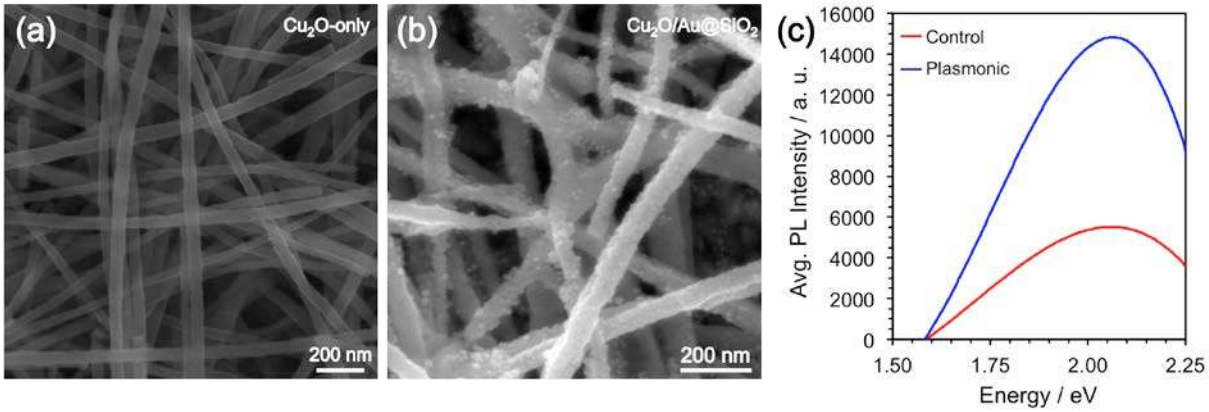

Figure S17. Average Photoluminescence (PL) Spectra of Control and Plasmonic Photocathodes

(a) SEM image of control (Cu_2O-only) photocathode. **(b)** SEM image of plasmonic (Cu_2O/Au@SiO_2) photocathode involving 10 nm Au nanoparticles coated with SiO_2 shells o 5 ± 2 nm. **(c)** Photoluminescence (PL) spectra for the control (Cu_2O-only) photocathode (black curve) and the plasmonic photocathode (blue curve) under 532 nm laser excitation. These data represent average PL signals taken from at least 9 different spots to remove sampling variability caused by film irregularity. A 532 nm laser was chosen to ensure simultaneous excitation of both the Cu_2O nanowires and the Au@SiO_2 nanoparticles. A broad PL signal centered at ca. 2.1 eV was observed for all devices, indicating that recombination in these nanowires occurs primarily by radiative recombination via electron-hole pairs near the band edge of Cu_2O (E_g ~2.0 eV). The incorporation of Au@SiO_2 nanoparticles into the device increases the PL emission of the Cu_2O nanowires by ca. 3 times compared to the control device.

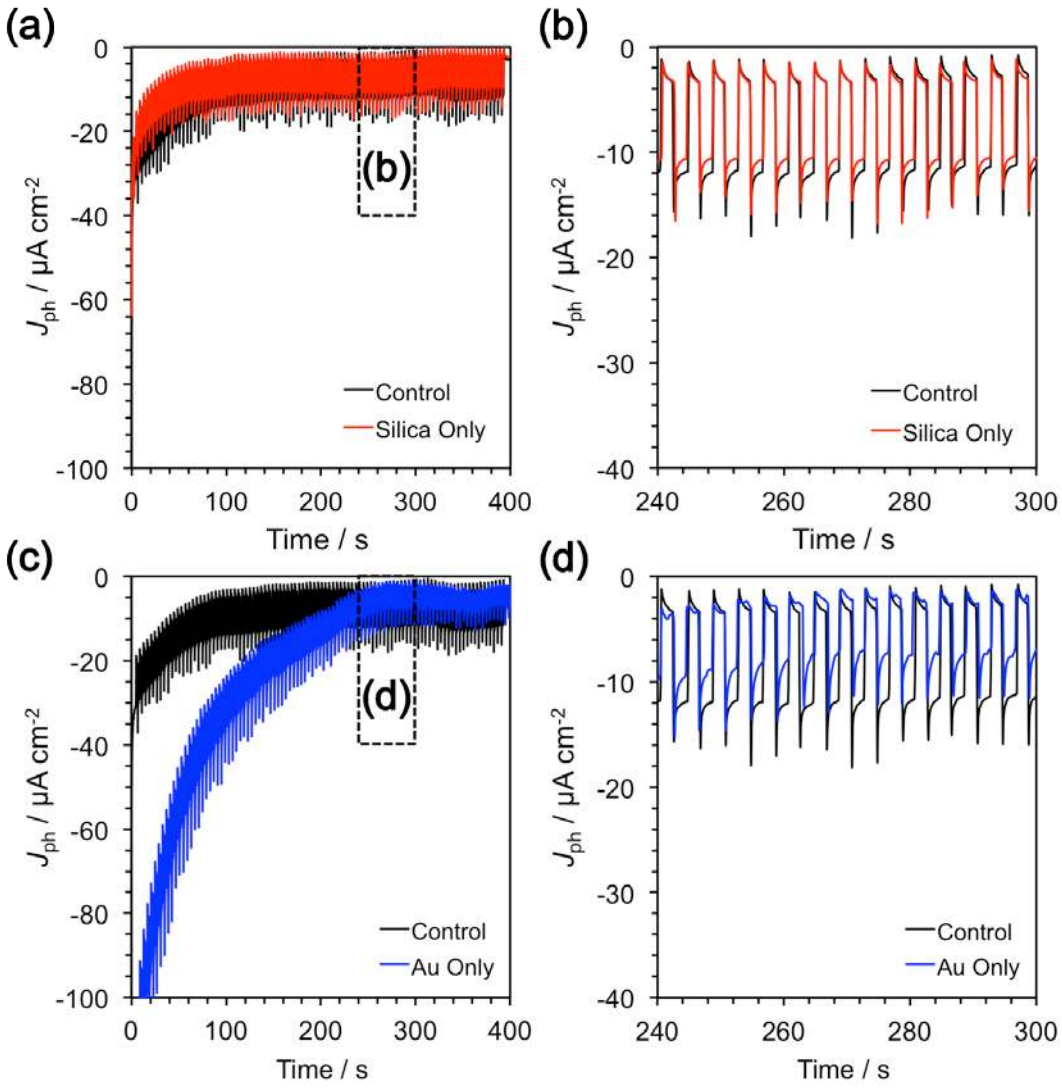

Figure S18. Photoelectrochemistry of Cu_2O/SiO_2 and Cu_2O/Au Photocathodes
Several control devices were also constructed to unequivocally identify the source of the enhancement provided by the Au@SiO_2 nanoparticles. Controlled potential electrolysis experiments were conducted under 1-sun AM 1.5G irradiation at 0 V_{RHE} for Cu_2O-based photocathodes containing **(a-b)** Au-only nanoparticles and **(c-d)** SiO_2-only nanoparticles. The introduction of 10 nm Au nanoparticles into the Cu_2O-only device substantially reduced the device performance (J_{ph} = −4 ± 1 μA cm^{-2}) when compared to the control (J_{ph} = −9 ± 1 μA cm^{-2}). We attribute this reduced J_{ph} to the high work function of the Au nanoparticles, which should act as electron sinks for photogenerated charge carriers and enhance recombination processes. This interpretation was later confirmed by PL measurements (see Figure S18). In contrast, the incorporation of 12 nm SiO_2 nanoparticles into the Cu_2O-only device exerted little effect on device performance (J_{ph} = −8 ± 1 μA cm^{-2}) compared to that of the control device (J_{ph} = −9 ± 1 μA cm^{-2}). This result suggests that the SiO_2 shell doesn't significantly influence the optoelectronic properties of the Cu_2O nanowires.

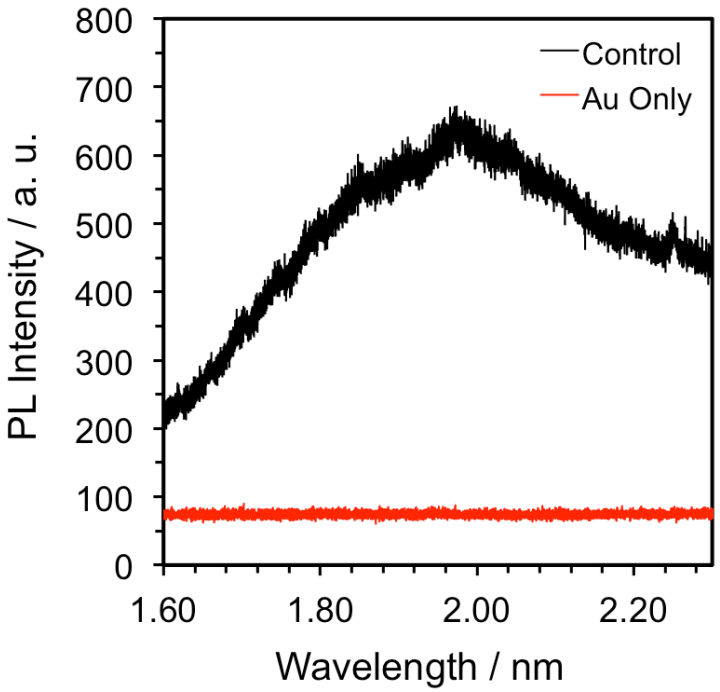

Figure S19. PL of Photocathodes with Uncoated Au Nanoparticles
The introduction of uncoated Au nanoparticles without SiO_2 shells into the Cu_2O-based device almost completely quenched the PL signal from the Cu_2O nanowires (red curve). This result confirms that the Au nanoparticles act as electron sinks to quench the excited state of the semiconductor within the nanowire network if not covered by an insulating SiO_2 shell.

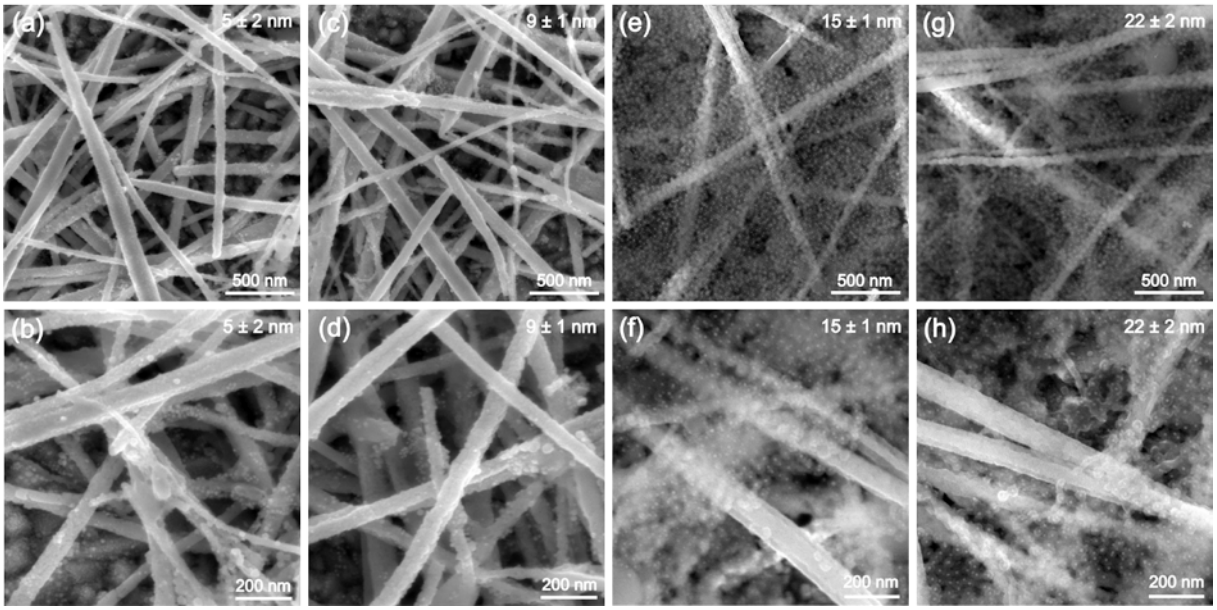

Figure S20. SEM Images of the Distribution of Au@SiO_2 Nanoparticles Encapsulated by Different SiO_2 Shell Thicknesses within Plasmonic Photocathodes

SEM images of plasmonic photocathode composed of Au@SiO_2 nanoparticles with different SiO_2 shell thicknesses: **(a,b)** 5 ± 1 nm SiO_2 shell, **(c,d)** 9 ± 1 nm SiO_2 shell, **(e,f)** 15 ± 1 nm SiO_2 shell, **(g,h)** 22 ± 2 nm. These images show that the drop-casting methods used for plasmonic photocathode fabrication provide a roughly homogeneous distribution of Au@SiO_2 nanoparticles embedded on and within the Cu_2O nanowire network. It is also apparent from these images that the thickness of the SiO_2 shell affects the distribution of these Au@SiO_2 nanoparticles within the nanowire networks. The Au@SiO_2 nanoparticles encapsulated by thicker SiO_2 shells tend to spread out over a larger area compared to those covered with thinner SiO_2 shells, as the thicker SiO_2 coatings prevent the Au cores from ever becoming too close together.

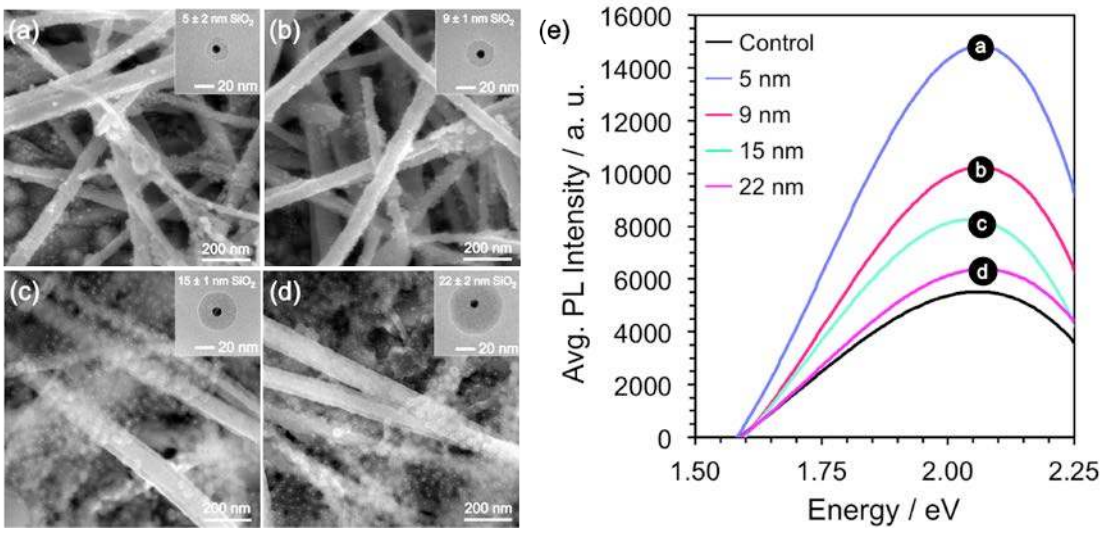

Figure S21. Influence of SiO_2 Shell Thickness on the Average Photoluminescence (PL) Signals Obtained from Plasmonic Photocathodes

(a-d) SEM images of plasmonic (Cu_2O/Au@SiO_2) photocathodes containing 10 nm Au nanoparticles coated with SiO_2 shells of various thickness: **(a)** 5 ± 2 nm, **(b)** 9 ± 1 nm, **(c)** 15 ± 1 nm, and **(d)** 22 ± 2 nm SiO_2 shells. Insets in images (a-d) show TEM imges of a signle Au@SiO2 core@shell nanoparticle representative of the batch used to prepare the plasmonic photocathodes. **(e)** Photoluminescence (PL) spectra for control (Cu_2O-only) photocathodes (black curve) and plasmonic photocathodes (Cu_2O/Au@SiO_2) as a function of SiO_2 shell thickness under 532 nm laser excitation. These data represent average PL signals taken from at least 9 different spots to remove sampling variability caused by film irregularity. A 532 nm irradiation wavelength was chosen to ensure simultaneous excitation of both the Cu_2O nanowires and the Au@SiO_2 nanoparticles. A broad PL signal centered at ca. 2.1 eV was observed for all devices, indicating that recombination in these nanowires occurs primarily by radiative recombination via electron-hole pairs near the band edge of Cu_2O (E_g ~2.0 eV).

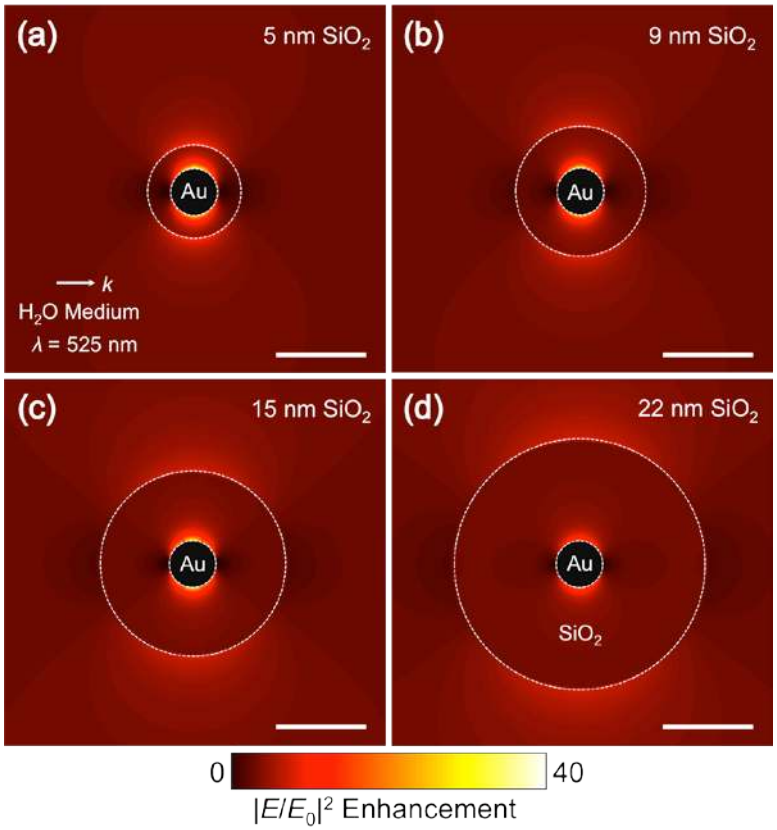

Figure S22. Electric Field Distribution around Au@SiO_2 Nanoparticles
DDA simulation results showing the spatial distribution of the electric field enhancement ($|E/E_0|^2$) around Au@SiO_2 nanoparticles coated with **(a)** 5 nm, **(b)** 9 nm, **(c)** 15 nm, and **(d)** 22 nm SiO_2 shells. The Au@SiO_2 nanoparticles were modeled as concentric spheres with physical dimensions congruent with those observed by TEM (Figure S7). A cursory inspection of these plots shows that the highest $|E/E_0|^2$ intensity was obtained for the Au@SiO_2 nanoparticles with the thinnest SiO_2 shell of 5 nm. These plots further show that these fields extend away from the SiO_2 surface into the surrounding water medium. Cu_2O nanowires within close proximity to these Au@SiO_2 nanoparticles should encounter these enhanced electric fields and exhibit increased photon absorption rates.

Supporting Information References

[1] S. Hacialioglu, F. Meng, S. Jin, *Chem. Commun.* **2012**, *48*, 1174.

[2] N. R. Jana, L. Gearheart, C. J. Murphy, *Langmuir* **2001**, *17*, 6782.

[3] J. S. DuChene, R. P. Almeida, W. D. Wei, *Dalton Trans*. **2012**, *41*, 7879.

[4] M. W. Kanan, D. G. Nocera, *Science* **2008**, *321*, 1072.

[5] B. H. Meekins, P. V. Kamat, *ACS Nano* **2009**, *3*, 3437.

[6] B. T. Draine, *Astrophys. J.* **1988**, *333*, 848.

[7] E. M. Purcell, C. R. Pennypacker, *Astrophys. J.* **1973**, *186*, 705.

[8] P. B. Johnson, R. W. Christy, *Phys. Rev. B* **1972**, *6*, 4370.

[9] J. Rodríguez-Fernández, I. Pastoriza-Santos, J. Pérez-Juste, F. J. García de Abajo, L. M. Liz-Marzán, *J. Phys. Chem. C* **2007**, *111*, 13361.

[10] Z. Zhang, R. Dua, L. Zhang, H. Zhu, H. Zhang, P. Wang, *ACS Nano* **2013**, *7*, 1709.

[11] A. Paracchino, N. Mathews, T. Hisatomi, M. Stefik, T. D. Tilley, M. Grätzel, *Energy Environ. Sci.* **2012**, *5*, 8673.

[12] J. Han, X. Zong, X. Zhou, C. Li, *RSC Adv.* **2015**, *5*, 10790.

[13] A. Azevedo, L. Steier, P. Dias, M. Stefik, C. T. Sousa, J. P. Araújo, A. Mendes, M. Grätzel, S. D. Tilley, *Energy Environ. Sci*. **2014**, *7*, 4044.

[14] P. Y. Chen, X. Dang, M. T. Klug, J. Qi, N.-M. D. Courchesne, F. J. Burpo, N. Fang, P. T. Hammand, A. M. Belcher, *ACS Nano* **2013**, *7*, 6563.

[15] A. Paracchino, J. C. Brauer, J.-E. Moser, E. Thimsen, M. Grätzel, *J. Phys. Chem. C* **2012**, *116*, 7341.

[16] P. T. Hsiao, Y. J. Liou, H. Teng, *J. Phys. Chem. C* **2011**, *115*, 15018.

[17] D. Bae, T. Pedersen, B. Seger, M. Malizia, A. Kuznetsov, O. Hansen, I. Chorkendorff, P. C. K. Vesborg, *Energy Environ. Sci.* **2015**, *8*, 650.